

ALD-Derived WO_{3-x} Leads to Nearly Wake-Up-Free Ferroelectric $\text{Hf}_{0.5}\text{Zr}_{0.5}\text{O}_2$ at Elevated Temperatures

Nashrah Afroze,^{*,†,‡} Jihoon Choi,^{*,‡,§} Salma Soliman,[†] Chang Hoon Kim,[‡] Jiayi Chen,[†] Yu-Hsin Kuo,[†] Mengkun Tian,[¶] Chengyang Zhang,[†] Priyankka Gundlapudi Ravikumar,[†] Suman Datta,^{†,§} Andrea Padovani,^{||} Jun Hee Lee,^{*,‡,⊥} and Asif Khan^{*,†,§}

[†]*Department of Electrical and Computer Engineering, Georgia Institute of Technology, Atlanta, GA-30332, USA.*

[‡]*School of Energy and Chemical Engineering, Ulsan National Institute of Science and Technology (UNIST), Ulsan-44919, South Korea.*

[¶]*Institute of Materials and Systems, Georgia Institute of Technology, GA-30332, USA.*

[§]*Department of Materials Science and Engineering, Georgia Institute of Technology, Atlanta, GA-30332, USA.*

^{||}*Department of Engineering Sciences and Methods (DISMI), University of Modena and Reggio Emilia, 42122 Reggio Emilia, Italy.*

[⊥]*Graduate School of Semiconductor Materials and Devices Engineering, Ulsan National Institute of Science and Technology (UNIST), Ulsan-44919, South Korea.*

[#]*These authors contributed equally to this work.*

E-mail: nafroze3@gatech.edu; jihoonchoi@unist.ac.kr; junhee@unist.ac.kr; akhan40@gatech.edu

Abstract

Breaking the memory wall in advanced computing architectures will require complex 3D integration of emerging memory materials such as ferroelectrics—either within the back-end-of-line (BEOL) of CMOS front-end processes or through advanced 3D packaging technologies. Achieving this integration demands that memory materials exhibit high thermal resilience, with the capability to operate reliably at elevated temperatures such as 125 °C, due to the substantial heat generated by front-end transistors. However, silicon-compatible HfO₂-based ferroelectrics tend to exhibit antiferroelectric-like behavior in this temperature range, accompanied by a more pronounced wake-up effect, posing significant challenges to their thermal reliability. Here, we report that by introducing a thin tungsten oxide (WO_{3-x}) layer—known as an oxygen reservoir—and carefully tuning its oxygen content, ultra-thin Hf_{0.5}Zr_{0.5}O₂ (5 nm) films can be made robust against the ferroelectric-to-antiferroelectric transition at elevated temperatures. This approach not only minimizes polarization loss in the pristine state but also effectively suppresses the wake-up effect, reducing the required wake-up cycles from 10⁵ to only 10 at 125 °C— a qualifying temperature for back-end memory integrated with front-end logic, as defined by the JEDEC standard. First-principles density functional theory (DFT) calculations reveal that WO₃ enhances the stability of the ferroelectric orthorhombic phase (o-phase) at elevated temperatures by increasing the tetragonal-to-orthorhombic phase energy gap, and promoting favorable phonon mode evolution, thereby supporting o-phase formation under both thermodynamic and kinetic constraints.

Keywords: Ferroelectric memory, HfO₂-based ferroelectrics, Oxygen reservoir layer, ALD deposited WO_{3-x}, High-temperature operation, Nearly wake-up-free, Memory-on-logic, 3D integration.

Introduction

AI is fueling advances across domains such as high-performance computing, cloud infrastructure, mobile platforms, autonomous vehicles, and augmented reality, yet the massive datasets

and complex models driving these applications are turning training and inference into critical memory and reliability challenges. Ferroelectric memory technologies, such as ferroelectric NAND (FE-NAND), ferroelectric random access memory (Fe-RAM), and ferroelectric field effect transistors (FeFETs) have become leading contenders for nonvolatile memory solutions across various segments of the memory hierarchy.¹⁻³ Recently, significant advancements in ferroelectric memories have been achieved, including the demonstration of a high-capacity dual-layer FE 1T-1C memory chip with a 32 Gb capacity and DRAM-comparable performance, as well as emerging three-dimensional integration of ferroelectric devices, exemplified by vertically stacked multi-layer ferroelectric architectures for high-density integration.^{4,5} Despite advantages such as non-volatility and high charge density, ferroelectric materials require a deeper understanding to ensure reliable operation, particularly under elevated temperatures.⁶

As the semiconductor industry advances toward 3D-IC integration, the intermediate step of memory-on-logic has demonstrated benefits comparable to a full technology node improvement. This memory-on-logic configuration shortens the communication distance between logic and memory, delivering up to 22% higher performance and 36% lower power consumption.⁷ However, thermal management poses a critical challenge. With an increasing number of stacked dies, tiers located farther from the heat sink and closer to heat-generating logic layers experience substantial thermal buildup due to thermal resistance and crosstalk⁸ (Figure 1a). Since logic dies are generally capable to operate at 105-125°C,⁹ memories must also be qualified to operate reliably at 125°C according to the JEDEC JESD22-A108 standard for 3D-IC qualification. Figure 1b summarizes the maximum operating temperature specifications of Micron DRAMs across different application scenarios.¹⁰ These specifications highlight the need for robust high-temperature performance, which is essential for enabling reliable integration of ferroelectric memories into emerging heterogeneous and monolithic 3D (H3D and M3D) systems and memory-on-logic architectures. Unfortunately, HfO₂-based ferroelectrics, which form the foundation of many next-generation memory devices, remain

highly vulnerable to performance degradation at elevated temperatures. It is well-established that increasing temperature induces an orthorhombic-to-tetragonal phase transition in ferroelectric materials, leading to pinching of the polarization loops and a gradual decrease in remnant polarization.^{11–17} Consequently, ferroelectricity can be lost under thermal stress, severely limiting device reliability.^{16,18–20} Although there has been lots of studies done on improving wakeup behavior and orthorhombic phase enhancement at room temperature using strategies like different atomic layer deposition (ALD) techniques,²¹ electrode engineering,^{22–25} controlling Oxygen flow during deposition,²⁶ high temperature cycling²⁷ and interface engineering,^{28–30} systematic efforts to improve wakeup effect and pristine state polarization at elevated temperatures remain scarce in the literature.³¹

Among various strategies to enhance ferroelectric device performance, interface engineering has shown particular promise. Several interfacial layers have been explored to improve endurance, leakage, and polarization characteristics. For example, NbO_2 and TiO_2 have been used for endurance enhancement,^{32–34} Pt has been employed to reduce leakage and wake-up effects,²⁶ and TiON and WN_x have been investigated for boosting polarization.^{29,35,36} More recently, WS_2 has demonstrated improvements in both polarization and endurance.³⁷ In particular, WO_x has gained attention as an effective oxygen reservoir for improving different properties of ferroelectric capacitors at room temperature.^{21,28,38–45} However, its potential for enhancing ferroelectric performance at elevated temperatures remains largely unexplored.^{46–48}

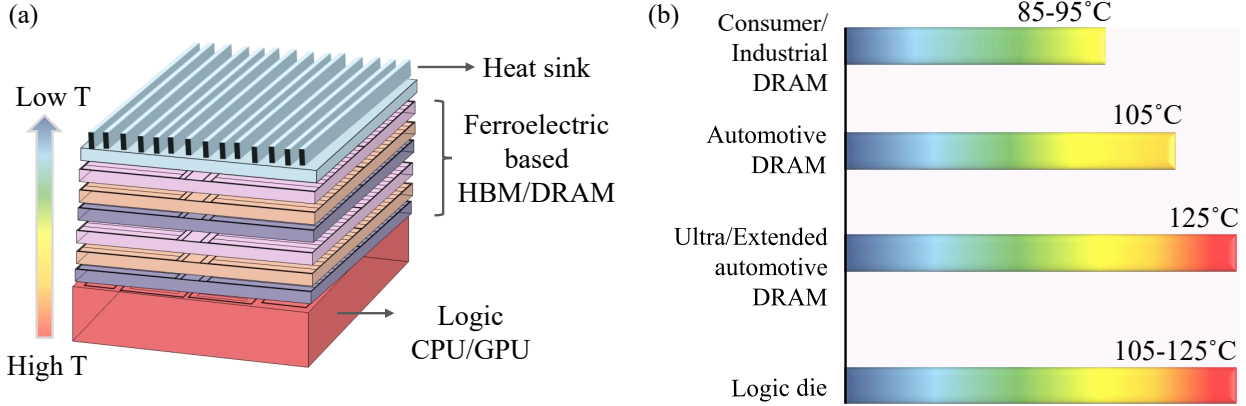


Figure 1: Importance of high temperature performance enhancement of ferroelectric memories. (a) Schematic of 3D integration of memory on logic architecture. Memories away from heat sink gets heated due to the heated logic die. (b) Operating temperatures of Micron DRAMs based on different applications.

In this study, we demonstrate that incorporating WO_{3-x} as an interfacial oxygen reservoir layer significantly enhances the high-temperature performance of $\text{Hf}_{0.5}\text{Zr}_{0.5}\text{O}$ (HZO)-based capacitors. WO_{3-x} is introduced at the interface between the bottom electrode and the HZO film, either by oxidizing the electrode via O_2 plasma treatment or through atomic layer deposition (ALD). This interface engineering approach increases the ability to retain orthorhombic phase in HZO, suppressing the emergence of antiferroelectric behavior in pristine devices under thermal stress. As a result, the number of bipolar cycles required to achieve wake-up is significantly reduced in WO_{3-x} -incorporated devices. First-principles density functional theory (DFT) calculations indicate that the presence of WO_3 stabilizes the ferroelectric o- phase at elevated temperatures through a combination of effects: an increased tetragonal-orthorhombic phase energy gap in the Helmholtz free energy landscape and enhanced X_2' phonon mode coupling. These effects arise from the lower entropy and lattice anisotropy induced by WO_3 , which together favor orthorhombic $\text{Pca}2_1$ phase formation under both thermodynamic and kinetic considerations. This stabilization of ferroelectric behavior under thermal stress enhances the temperature resilience of the device. Our results provide a promising pathway for achieving thermally robust ferroelectric memories, such as Fe-RAMs and Fe-FETs, enabling their deployment in emerging 3D memory-on-logic

architectures where elevated temperatures present a significant reliability challenge.

Results and discussion

Experiment

Figure 2a illustrates the fabrication process flow of ferroelectric capacitors incorporating WO_{3-x} as an oxygen reservoir layer, introduced via two distinct methods. In the first approach, partial oxidation of the sputtered W bottom electrode on Si was carried out using O_2 plasma treatment within the atomic layer deposition (ALD) chamber, resulting in the formation of an approximately 4 nm thick WO_{3-x} layer at the W surface. In the second approach, a plasma-enhanced ALD (PE-ALD) technique was employed to directly deposit 5 nm and 6 nm thick WO_{3-x} layers on the W electrode. For the reference device, the HZO layer was deposited directly on the bottom W electrode without any intermediate WO_{3-x} layer. Further details of the fabrication procedure are described in the *Methods* section.

Scanning transmission electron microscopy (STEM) images of the cross-section of the fabricated devices are presented in the left most panel of Figures 2b–d, corresponding to the reference, O_2 plasma, and ALD-based WO_{3-x} device structures, respectively. To verify the formation of WO_{3-x} at the bottom interface in both the O_2 plasma and ALD-based devices, energy-dispersive X-ray spectroscopy (EDS) was carried out. Elemental mapping confirmed the presence of distinct W and O signals at the interface in these devices, validating the successful formation of a WO_{3-x} layer. In contrast, the reference device exhibited no such signals, indicating the absence of an interfacial WO_{3-x} layer.

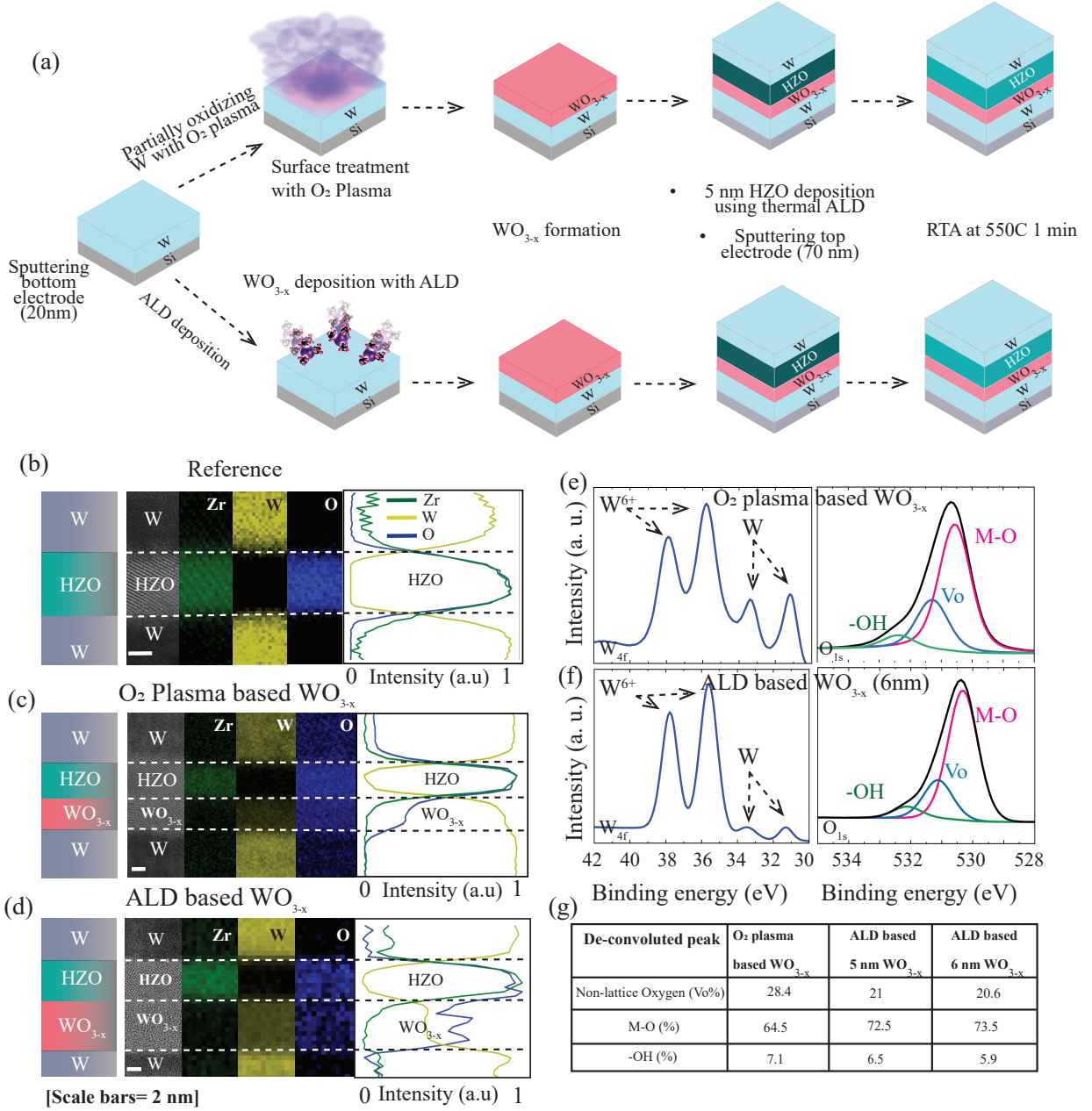


Figure 2: Device structures and material characterization of ferroelectric capacitors. (a) Fabrication process of O₂ plasma and ALD based WO_{3-x} devices. (b-d) Cross-sectional STEM images of (b) reference, (c) O₂ plasma and (d) ALD based 6 nm WO_{3-x} devices along with their EDS characterization. Material-count map coming from Zr (green), W (yellow) and O (blue) and the corresponding line scans for (b) reference, (c) O₂ Plasma and (d) ALD devices. The line scans on the right of each material count map further confirms the layers and their interfaces. XPS spectra obtained from W 4f and O 1s orbitals of WO_{3-x} from (e) O₂ plasma and , (f) ALD based 6nm WO_{3-x} samples. (e,f) Magenta, blue and green curves in the O 1s plot are the de-convoluted peaks corresponding to M-O, non-lattice Oxygen (V_o) and -OH respectively. (g) Table showing the percentage obtained from the deconvoluted peaks of O 1s scan of different samples.

To assess the stoichiometry of WO_{3-x} films synthesized via O_2 plasma treatment and atomic layer deposition (ALD), X-ray photoelectron spectroscopy (XPS) analysis was conducted, as shown in Figures 2e and 2f. The W 4f spectra from both samples exhibit prominent W^{6+} peaks, confirming the successful formation of WO_{3-x} . The O 1s spectra were deconvoluted to quantify the contributions from lattice and non-lattice oxygen species, with the extracted component ratios summarized in Figure 2g. Notably, the O_2 plasma based WO_{3-x} film shows a significant contribution from non-lattice oxygen, corresponding to an oxygen vacancy (V_o) concentration of approximately 28.4%. In contrast, the ALD-deposited WO_{3-x} films with 5 nm and 6 nm thicknesses exhibit a comparatively lower V_o concentration of 21%. The full XPS spectrum for the 5 nm ALD-grown WO_{3-x} is provided in Figure S1. These results indicate that while both methods yield substoichiometric WO_{3-x} , the O_2 plasma process introduces a higher density of oxygen vacancies. Furthermore, these findings underscore that the deposition technique, rather than film thickness, plays a critical role in governing WO_{3-x} stoichiometry, which in turn significantly impacts the electrical behavior of the devices, as elaborated in Figure 3.

Figure 3 presents the polarization–voltage (P–V) characteristics of all fabricated devices, along with the extracted coercive voltage and remnant polarization values from P–V and positive-up negative-down (PUND) measurements respectively. To decouple ferroelectric switching from leakage effects, PUND measurements were performed. All devices demonstrated comparable remnant polarization ($2P_r$), confirming that the incorporation of WO_{3-x} does not compromise ferroelectric polarization. Additionally, WO_{3-x} plays a beneficial role in enhancing device endurance, both at room and at higher temperatures, as shown in Figure S2 and supported by previous studies.^{39,41} A detailed analysis of temperature-dependent endurance improvements due to WO_{3-x} incorporation can be found in earlier work.⁴⁶ Moreover, the inclusion of WO_{3-x} does not adversely affect imprint and retention behavior, as illustrated in Figure S3 and S4.

The coercive voltage of the O_2 plasma based device closely matches that of the reference

device, whereas the ALD-deposited WO_{3-x} devices exhibit higher coercive voltage (Figure 3). This behavior indicates that the ALD-deposited WO_{3-x} is less conductive compared to the plasma based counterpart, thereby dropping more voltage across the WO_{3-x} layer and requiring a higher switching voltage for the overlying HZO layer. This increase in coercive voltage is consistent with the comparatively lower conductivity measured on these devices (Figure S5), and the lower oxygen vacancy (V_{o}) concentration observed in the ALD samples from the XPS analysis in Figures 2e–g. Given that oxygen vacancies significantly affect the electrical conductivity of WO_3 films,^{45,49} the reduced V_{o} content in ALD-deposited layers leads to decreased conductivity.

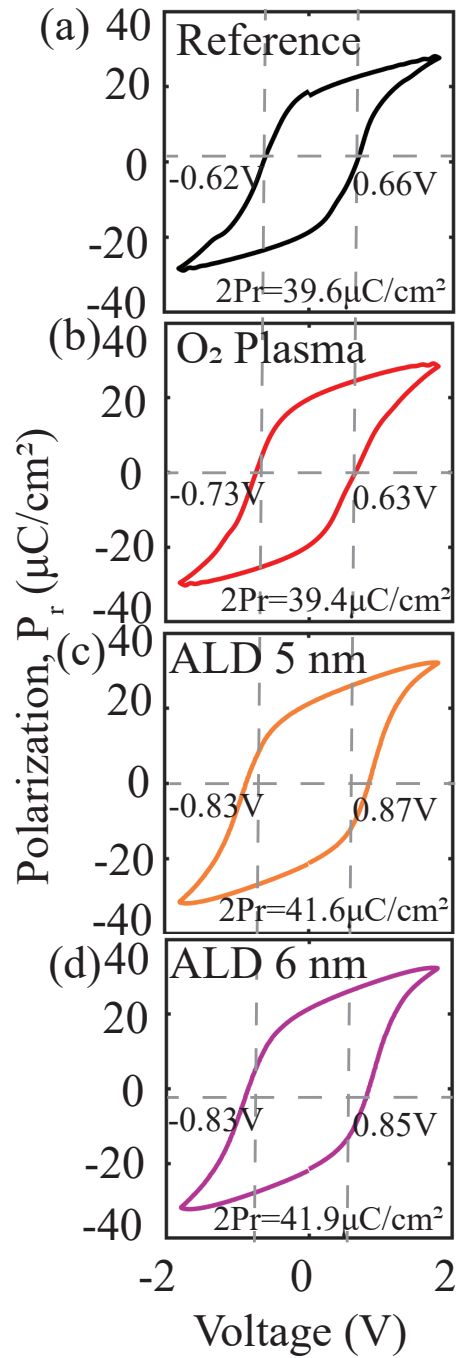


Figure 3: Electrical characterization at room temperature. PV loops after 10^5 cycles from (a) reference, (b) O₂ plasma-, ALD based (c) 5 nm and (d) 6 nm WO_{3-x} devices. $2P_r$ values are extracted from PUND measurement.

The polarization–voltage (P–V) and switching current–voltage (I_{sw}–V) characteristics of all three devices in their pristine states were measured across a wide range of tempera-

tures, as shown in Figure 4. At room temperature, both the reference and the O₂ plasma based WO_{3-x} devices exhibit similar P–V and I_{sw}–V responses, while the ALD-deposited WO_{3-x} device shows marginally enhanced ferroelectric behavior (Figures 4a–c). Upon increasing the temperature to 85°C, the reference device that lacks any WO_{3-x} interfacial layer exhibits a pronounced antiferroelectric-like response, evidenced by a well-defined double-peak structure in the I_{sw}–V curve (Figure 4d), indicating that the transition away from the orthorhombic ferroelectric phase initiates well before the targeted operating temperature (125°C) is reached.

In contrast, the O₂ plasma based device demonstrates improved thermal stability of ferroelectricity, evidenced by reduced separation of switching current peaks compared to reference device at 85°C (Figure 4e). A smaller separation between same-direction switching peaks indicates reduced antiferroelectric-like behavior.⁵⁰ Further enhancement in thermal robustness is observed for devices with ALD based WO_{3-x} for the 6 nm layer (Figure 4f) and similarly for the 5 nm variant (Figure S6). These devices show a minor residual switching peak on the negative voltage side across all temperatures, suggesting that WO_{3-x} incorporation effectively suppresses or delays the onset of the antiferroelectric phase transition.

This trend is validated by PUND measurements performed under varying temperature conditions at pristine states. Using 200 ns square pulses of varying amplitudes, the switched polarization (2P_{sw}) was extracted. At room temperature, all devices exhibit comparable saturated polarization values in pristine condition (Figure 4g). However, at 125°C, the reference device shows a significant drop in polarization relative to the WO_{3-x}-containing devices (Figure 4h), indicating temperature-induced degradation of ferroelectricity in the absence of WO_{3-x}. This observation is further reinforced by long-pulse (10 μs/2V) PUND measurements across a wide temperature range on pristine devices, where the extracted 2P_r values confirm that ferroelectric property deteriorates significantly in the reference device, while devices with WO_{3-x} maintain polarization more effectively (Figure 4i). These results highlight the crucial role of WO_{3-x} in stabilizing the ferroelectric orthorhombic phase at elevated

temperatures at pristine state, thereby preserving ferroelectric properties and suppressing unwanted phase transitions.

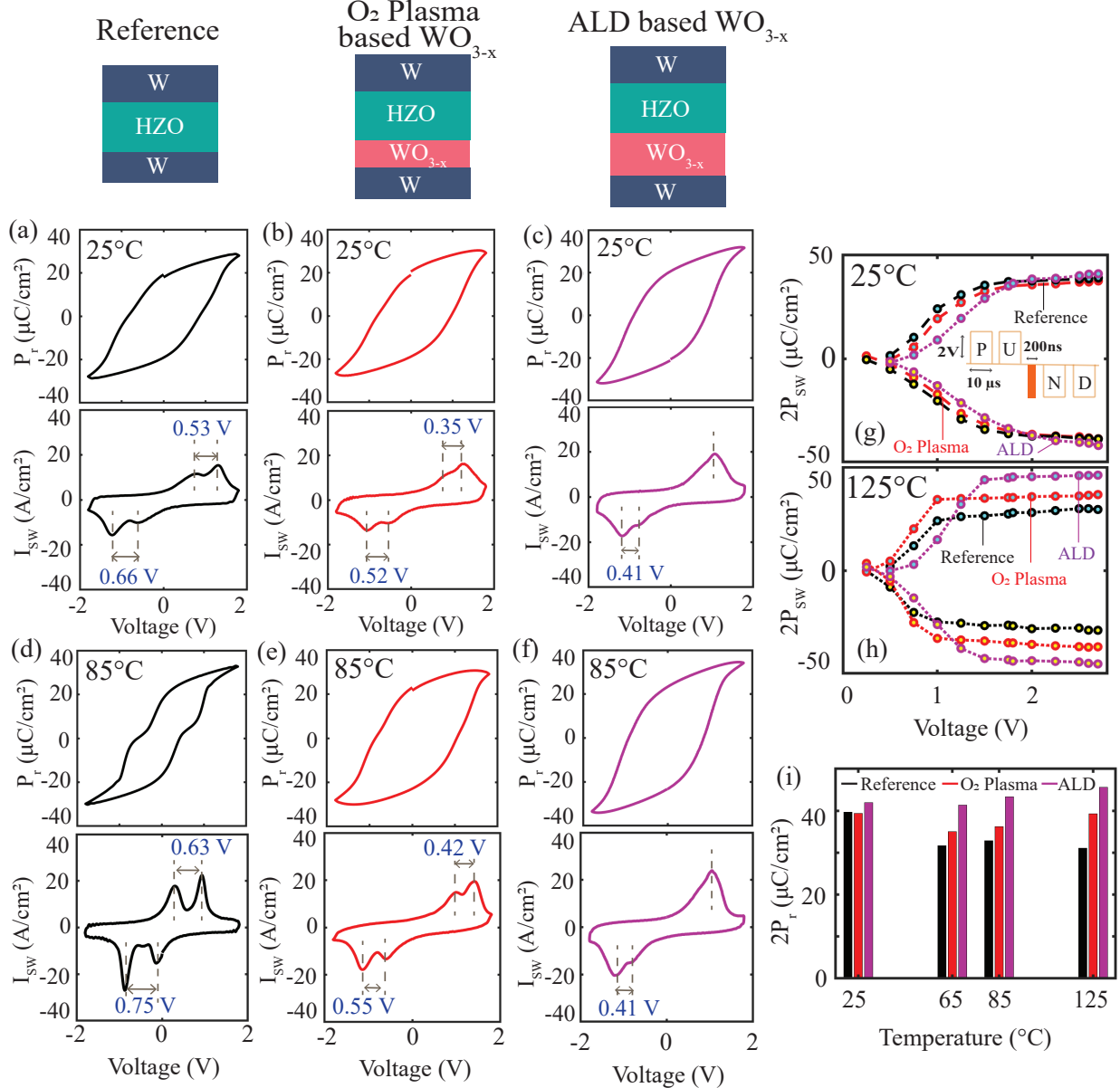


Figure 4: Temperature dependent polarization and switching current characteristics at pristine state. P - V and I_{SW} - V characteristics at (a-c) 25 and (d-f) 85°C from (a,d) reference, (b,e) O_2 plasma- and (c,f) ALD- based WO_{3-x} devices respectively. (g-h) Polarization switched with 200ns pulses at different voltages measured at 25 and 125°C respectively on pristine devices. (i) $2P_r$ obtained from PUND measurement with 2V/10 μ s square pulses at different temperatures at pristine state.

To confirm the stabilization of the ferroelectric α - phase with the incorporation of WO_{3-x}

at elevated temperatures, grazing incidence X-ray diffraction (GI-XRD) measurements of the HZO layer in reference, O₂ plasma and ALD based WO_{3-x} samples were performed at 25, 85, and 125°C. As shown in Figure 5a, the major o-(111)/t-(101) diffraction peak through Gaussian fitting from the samples having WO_{3-x} are shifted toward lower angles compared to the reference device, indicating a greater orthorhombic phase fraction. This observation aligns with the known peak positions of the o-(111) and t-(101) phases in HZO, located at approximately 30.4° and 30.8°, respectively. At 85°C, the peak separation between these samples decreases; however, the samples having WO_{3-x} still exhibit a discernible shift toward the orthorhombic phase, suggesting that a greater proportion of the orthorhombic phase is retained relative to the reference sample (Figure 5b). This behavior persists at 125°C, as shown in Figure 5c. The phase fractions of the o- and t- phases, extracted from the deconvolution of the o-(111)/t-(101) peaks measured at 125 °C, are shown in Figure S7. The evolution of the peak positions with temperature for all the samples is summarized in Figure 5d.

These results clearly demonstrate that the incorporation of WO_{3-x} helps maintain a higher orthorhombic phase fraction across a wide temperature range. And one of the reasons for this could be better lattice matching between orthorhombic Pca₂₁ HZO and monoclinic WO₃ compared to that with W (Table S1). Monoclinic phase of WO₃ is chosen for comparison, as this phase is confirmed by STEM imaging of the O₂ plasma device (Figure S8). Additionally, the optimized Vo concentration in ALD-deposited WO_{3-x} is likely to promote enhanced o-phase stability in HZO compared to O₂ plasma based WO_{3-x}, as prior studies have shown that stabilization of the o- phase in HZO is maximized within an optimal vacancy window in WO_{3-x}, whereas both excessively vacancy-rich and near-stoichiometric (vacancy-poor) conditions lead to reduced o-phase content.^{45,51} The enhanced ferroelectric o-phase stability plays a critical role in suppressing the transition to antiferroelectric-like behavior at elevated temperatures, thereby contributing to improved ferroelectric performance.

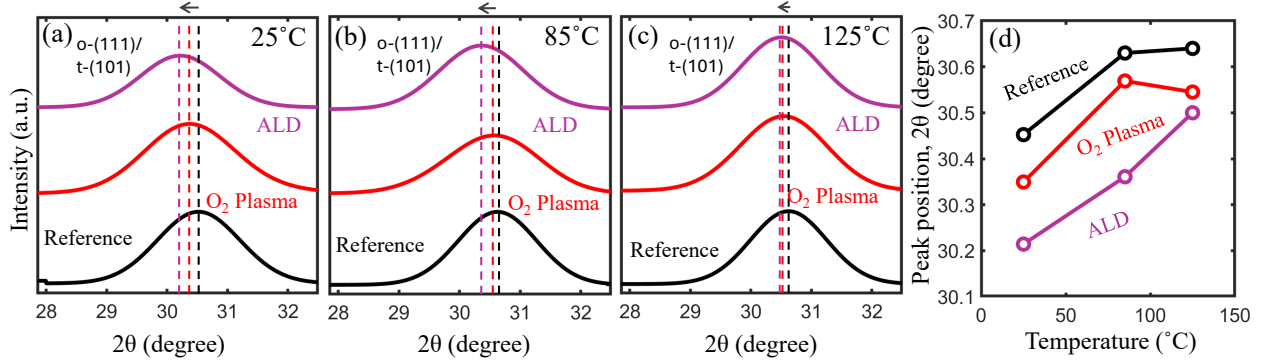


Figure 5: Grazing incident X-ray diffraction (GI-XRD) from the HZO film of reference, O₂ plasma and ALD based 6 nm WO_{3-x} samples at (a) 25, (b) 85 and (c) 125°C. (d) Dominant peak (o-111/t-101) position of all the samples at different temperatures obtained from (a)-(c).

The influence of electrical cycling on the switching behavior, with and without the presence of a WO_{3-x} interfacial layer at elevated temperatures, is studied in Figure 6. For the reference device, which lacks WO_{3-x}, a significant number of cycles-10⁴ at 85°C and 10⁵ at 125°C are required to suppress the characteristic double peaks in the I_{sw} response and achieve clean ferroelectric switching (Figures 6a–b). In contrast, the O₂ plasma based WO_{3-x} device exhibits stable ferroelectric switching behavior earlier than reference, showing a single peak in the I_{sw} profile after just 10³ and 10⁴ cycles at 85 and 125°C, respectively (Figures 6c–d).

Remarkably, for the ALD based 6 nm WO_{3-x} device, as few as 10 cycles are sufficient for transition to pure ferroelectric switching at both 85 and 125°C (Figures 6e–f). This phenomena is true for ALD based 5 nm WO_{3-x} device as well (Figure S9). The substantial reduction in wake-up cycles observed in ALD-based WO_{3-x} compared to O₂ plasma based WO_{3-x} devices is consistent with the inherently gentler nature of the ALD process, which proceeds through self-limiting surface reactions and minimizes plasma-induced surface and interfacial defect generation. Collectively, these results underscore the critical role of the WO_{3-x} interfacial layer in enhancing the thermal and electrical stability of the ferroelectric phase. The corresponding P–V loops at 85 and 125°C after different cycling stages are shown in Figures 6(g–l) for reference, O₂ plasma and 6nm ALD WO_{3-x} devices and in Figure S10

for 5nm ALD WO_{3-x} device, further corroborating these trends. It is worth noting that once pure ferroelectric switching is achieved in the ALD based WO_{3-x} devices at high temperatures after 10 bipolar cycles, it remains well preserved upon cooling to room temperature (Figure S11). Table 1 presents a benchmark of the 6 nm ALD WO_{3-x} device against prior studies on high-temperature ferroelectric capacitor behavior. The results indicate that the ALD WO_{3-x} device achieves superior pristine polarization and undergoes significantly fewer wake-up cycles during elevated-temperature operation compared with recent reports. The $2P_r$ values of this work are obtained from the PUND measurement of Figure 4i.

The leakage current density and trap generation rate with electrical cycling of all devices at different temperatures are presented in Figure S12. Although all the devices including reference device show similar trap generation rate at room temperature, WO_{3-x} containing devices show a significantly lower trap generation rate during electrical cycling at elevated temperatures, irrespective of the WO_{3-x} deposition method (Figure S12(d–f)). This reduced trap generation is attributed to the oxygen-reservoir function of the WO_{3-x} layer, which contributes to the improved endurance (as shown in Figure S2) observed in these devices.⁴⁷

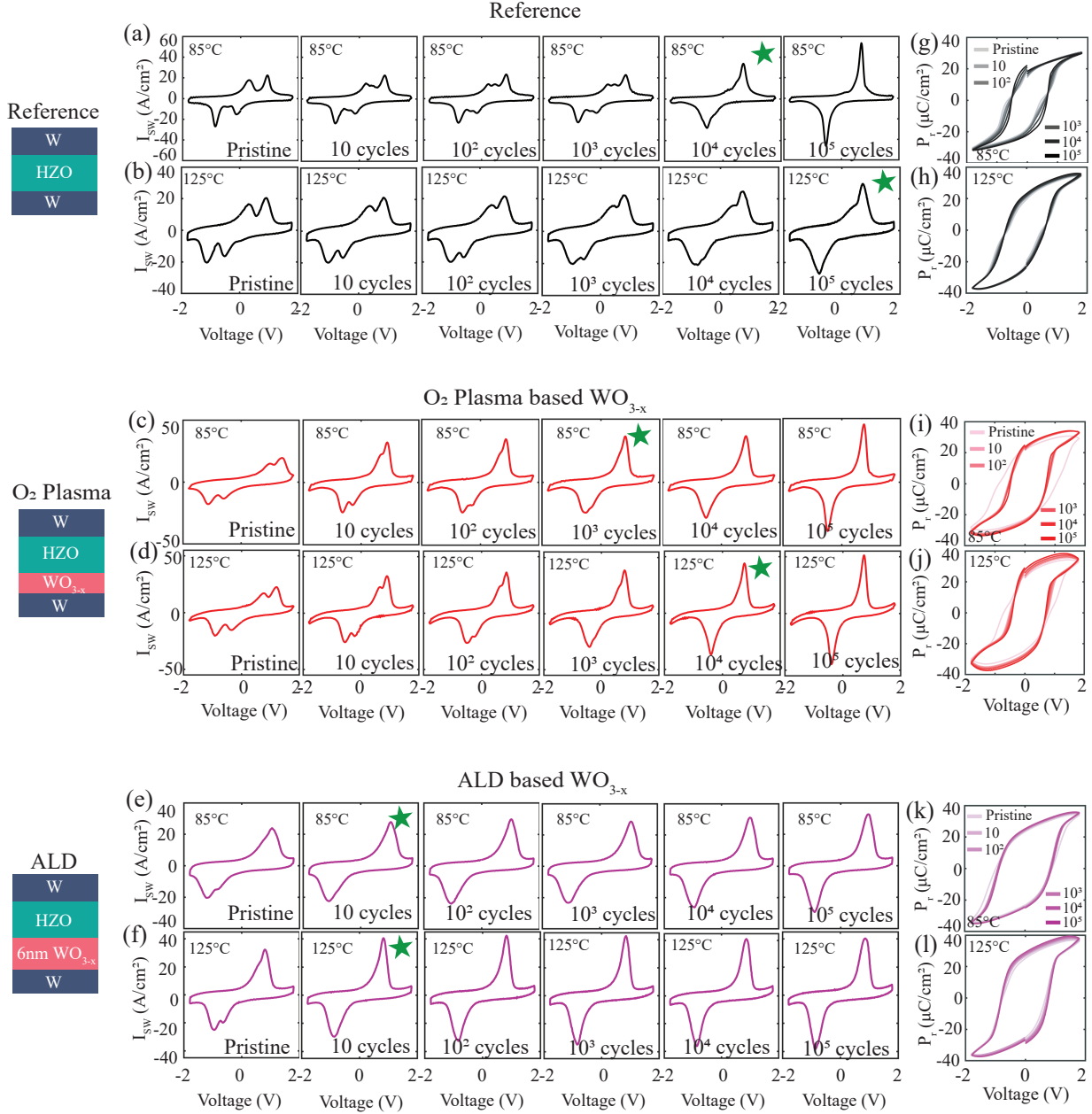


Figure 6: Temperature and cycling dependent P-V and I_{SW}-V characteristics. I_{SW}-V characteristics at (a,c,e) 85 and (b,d,f) 125°C from pristine to 10⁵ cycles for (a-b) reference, (c-d) O₂ plasma based WO_{3-x} and (e-f) ALD based WO_{3-x} device. Green asterisks denote the number of cycles which are required to remove the anti-ferroelectric like double peak behavior. P-V loops from pristine to 10⁵ cycles at (g,i,k) 85 and (h,j,l) 125°C of (g-h) reference, (i-j) O₂ plasma based WO_{3-x} and (k-l) ALD based WO_{3-x} device.

Table 1: Comparison of ferroelectric properties at high temperature (HT) with prior works.

	[29]	[16]	[17]	[25]	[45]	This work
Film thickness (nm)	10	10	7	3	12	5
Write Voltage (V)	3.5	2.2	2.1	1	3	1.8
Electric field (MV/cm)	3.5	2.2	3	3.3	2.5	3.6
Pristine $2P_r$ ($\mu\text{C}/\text{cm}^2$)	26	15.1	16	5	32.94	41.94
Pristine $2P_r$ at HT ($\mu\text{C}/\text{cm}^2$)	–	7 (120°C)	13.56 (125°C)	11.81 (85°C)	24.95 (100°C)	45.57 (125°C)
Cycles to wakeup at HT	10^3 (100°C)	10^6 (100°C)	10^4 (100°C)	10^3 (85°C)	10^6 (100°C)	10 (125°C)

Density functional theory (DFT)

To investigate the origin of the stabilization of ferroelectric properties at elevated temperatures in the presence of WO_{3-x} , density functional theory (DFT) calculations were performed to compare the stability of the orthorhombic Pca_{21} phase in HZO when deposited on W and WO_3 . In this analysis, the atomic structure of bulk HZO was strained to match the lattice parameters of W and WO_3 , as illustrated in Table S1. Although the Tungsten oxide layer in the fabricated ferroelectric capacitors is sub-stoichiometric, HZO lattice is strained to WO_3 lattice for the calculation as the dominant feature in the W 4f XPS spectra corresponds to W^{6+} oxidation state. Furthermore, WO_{3-x} containing oxygen vacancies does not exhibit a single well-defined periodic lattice constant due to the configurational disorder introduced by these vacancies. To account for oxygen deficiency, lattice mismatch calculations were carried out using WO_3 supercell containing a single oxygen vacancy, as summarized in Table S1. The mismatch values indicate that oxygen vacancies can tune the cell-averaged mismatch while primarily introducing local strain inhomogeneity.⁵² However, the key thermodynamic and kinetic trends discussed henceforth remain qualitatively unchanged.

Figure 7a presents the Helmholtz free energy of HZO in the monoclinic (m-), tetragonal (t-), and o- phases, each strained to match the lattice parameters of W and WO_3 , respectively. The yellow-shaded region indicates the high operating temperature range of interest (65–125 °C). Within this range, the energy difference between the t- and o-phases of HZO strained to the WO_3 lattice increases by approximately 20% compared to that strained to the W lattice, thereby favoring formation of the o-phase in the WO_3 case. This behavior arises because

W, having a cubic structure, induces a more cubic-like configuration in HZO, resulting in higher entropy relative to the WO_3 lattice (as reflected by the slope of the Helmholtz free energy curve). Consequently, the energy gap between the t- and o-phases is larger for WO_3 at elevated temperatures. While W exhibits a greater lattice mismatch and thus higher surface energy than WO_3 , the increase in surface energies for both the o- and t-phases is comparable, yielding only a minor overall effect on the Helmholtz free energy.

Although the m-phase remains the thermodynamically most stable state even at a film thickness of 5 nm (i.e., exhibiting the lowest Helmholtz free energy), the kinetic barrier for the $\text{t} \rightarrow \text{o}$ phase transition is substantially lower than that for the $\text{t} \rightarrow \text{m}$ transition. Consequently, under kinetic constraints, the system preferentially transforms into the o-phase rather than the m-phase,⁵³ in agreement with the calculations presented in Table S2. During cooling, the high energy barrier similarly suppresses the formation of the m-phase, leading to the preferential development of the o-phase, which possesses a lower Helmholtz free energy than the t-phase. This trend is further supported by Figure 7a, where the o-phase remains more stable than the t-phase even at elevated operating temperatures, making it the energetically favorable configuration.

As shown in Figure 7b, t-phase of HZO exhibits only the X_2' oxygen phonon mode, which drives the cubic-to-tetragonal phase transition. When strain is applied to match the lattice constant of WO_3 , corresponding to an approximately 1.7% increase in the lattice constant along the x-direction relative to the pristine structure, the X_2' phonon mode in the t-phase is enhanced. This enhancement brings its value closer to that of the o-phase, indicating that the $\text{t} \rightarrow \text{o}$ phase transition becomes more accessible. Under W lattice, the larger lattice mismatch produces a greater amplitude of the X_2' mode compared to the WO_3 case, leading, as shown in Table S2, to a lower $\text{t} \rightarrow \text{o}$ transition energy barrier. Overall, while the larger strain induced by W reduces the transition barrier relative to WO_3 , the o-phase in the WO_3 case remains thermodynamically more stable than the t-phase due to the combined effects of surface energy at the 5 nm thick HZO and the large entropy associated with the larger

in-plane lattice matched to the W cubic structure under non-equibiaxial strain (as described in Figure S13). These results are consistent with previous phase stabilization studies for the ZrO_2 – WO_3 interface.⁴²

The polarization switching barrier of HZO strained to the W and WO_3 lattices were further calculated and found to be lower in the WO_3 -strained case (Figure S14). This difference arises because, in the switching pathway, the transition state corresponds to the t-phase, which exhibits a longer lattice constant along the x-direction than along the y-direction. For W, the structure is more cubic-like, with nearly identical lattice constants in both directions, leading to a higher switching barrier. In contrast, the anisotropy in the WO_3 -strained lattice reduces the barrier height. This energy barrier difference contributes to improved overall switching kinetics in devices incorporating WO_3 or WO_{3-x} as the interfacial layer.

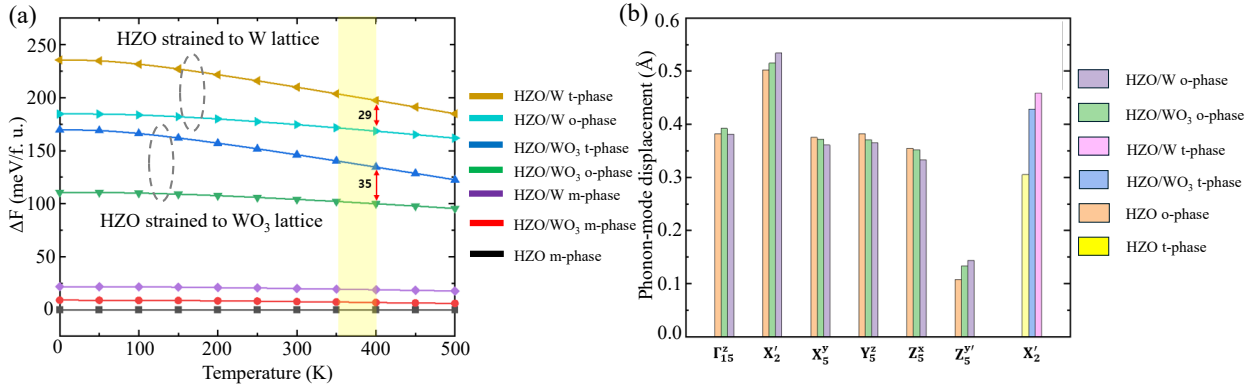


Figure 7: Density functional theory (DFT) analysis. (a) Helmholtz free energy difference (ΔF) for the 5 nm HZO film, relative to the m- phase. The yellow region and red arrow indicate the high-temperature operating range and free energy difference between t- and o- phase under W and WO_3 -induced strain. (b) Phonon mode analysis under tensile strain induced by W and WO_3 , where the enhancement of the soft X_2' mode in the t-phase induces the phase transition to the o-phase.

Conclusion

In this study, we demonstrated the critical role of WO_{3-x} interfacial layer in enhancing the thermal stability and ferroelectric performance of ultrathin $\text{Hf}_{0.5}\text{Zr}_{0.5}\text{O}_2$ (HZO)-based capac-

itors. The incorporation of WO_{3-x} , regardless of the deposition method and with carefully tuned oxygen vacancy, effectively suppressed the transition toward antiferroelectric-like behavior at elevated temperatures and enabled nearly wakeup-free operation with significantly fewer bipolar cycles. This improvement is attributed to the reduced relative Helmholtz energy for the orthorhombic phase in the presence of WO_{3-x} , which favors the retention of ferroelectric properties even under thermal stress. These findings offer a promising pathway toward the realization of robust ferroelectric memories suitable for 3D memory-on-logic architectures, where reliable high-temperature operation is essential.

Methods

Device fabrication

Ferroelectric HZO capacitors were fabricated on p^+ $\text{Si}(100)$ substrates with a doping concentration of 10^{20} cm^{-3} . A 20 nm W bottom electrode was deposited using a Unifilm sputter system at a deposition rate of 200 \AA . 5 nm HZO layer was deposited using the Kurt J. Lesker ALD tool at 250°C using TDMAH and TDMAZ precursors for Hf and Zr, and H_2O as oxidant in the Th-ALD process -directly on W in case of reference sample. For the O_2 plasma sample, the W electrode was oxidized to form a WO_{3-x} interfacial layer through 10 cycles of Oxygen plasma treatment in the ALD chamber prior to HZO deposition, ensuring no vacuum break. For the ALD WO_{3-x} samples, 20 and 30 cycles of ALD were used to deposit 5 nm and 6 nm WO_{3-x} layers respectively before depositing HZO in Veeco Fiji G1 ALD system with a Bis(tert-butylimino)bis(dimethylamino) (BTBMW) tungsten precursor and O_2 plasma (300 W power, 40 sccm O_2 flow, and 5s plasma exposure per cycle) as oxidant at 250 °C. 70 nm W top electrode was sputtered onto all devices, followed by rapid thermal annealing (RTA) at 550°C for 1 minute in N_2 atmosphere. Finally, standard photolithography and dry etching were used to define $50 \mu\text{m} \times 50 \mu\text{m}$ capacitor structures.

Energy-dispersive X-ray spectroscopy (EDS)

The EDS maps were collected using a Bruker E3DS detector with a 60 mm^2 window, on cross-sectional focused ion beam (FIB)-prepared samples in a Hitachi HD-2700 STEM. The spectra was then read via Hyperspy and background subtractions were performed by selecting one window before and one window after the peaks of interest. Peaks corresponding to Zr-K α , W-L α , and O-K α were used for mapping. To denoise the spectra, principal component analysis (PCA) was first applied, retaining four components, and then Online Robust Nonnegative Matrix Factorization (ORNMF) was performed using these four components identified. Line scan were created at the center of horizontal direction (x axis) for each map with a width of 40 pixels.

X-ray photoelectron spectroscopy (XPS)

X-ray photoelectron spectroscopy (XPS) was conducted after depositing WO_{3-x} (either by ALD or using O_2 plasma) on sputtered bottom W electrode on Si substrate. Thermo K-alpha XPS System with an Al K α x-ray source and a beam spot size of $200\text{ }\mu\text{m}$ was used for the scan. Flood gun was always on during the data acquisition. XP emission peaks are charge corrected to the carbon 1s peak which is set at 284.8 eV. XP emission backgrounds are subtracted with Shirley algorithm, and the peaks are fitted with Powell algorithm, with convergence level < 0.0001 .

Grazing incident X-ray diffraction (GI-XRD)

After removing top electrode of the devices using W etchant, GIXRD scan was done using a RIGAKU Smartlab XE diffractometer equipped with a Cu K α source (40kV, 50mA) and a HyPix-3000HE detector. In-situ high temperature data is collected on RIGAKU Reactor X stage. Data was acquired in the range of 27° - 34° , with an incidence angle of 0.5° , scanning step of 0.04° , and scanning speed of $0.05^\circ/\text{min}$. O and T peaks are constrained to have

gaussian shape and same FWHM when deconvolution.

Electron Microscopy

Cross-sectional samples for scanning transmission electron microscopy (STEM) imaging and EDS were prepared using a Thermo Fisher Helios 5CX FIB/SEM equipped with a high energy Focused Ion Beam (FIB) using Gallium-69 and operated at an accelerating voltage between 0.1 and 30 kV. The final polishing condition was performed at 10 pA at 2kV. A Hitachi HD-2700 aberration- corrected STEM/SEM was used to capture STEM images, operated at a 200 kV accelerating voltage and 27 mrad convergence semi-angle. The spatial resolution was about 1.3 Å.

Electrical measurements

Electrical measurements were performed using a Cascade Microtech Summit 1200K semi-automated probe station, equipped with a Keysight B1500 semiconductor device analyzer. A $20\ \mu\text{s}$ triangular pulse with an amplitude of 1.8 V was applied to measure the P-V and I_{SW} -V characteristics. For bipolar cycling, 200 ns pulses with an amplitude of 1.8 V were used. PUND measurements were conducted using $10\ \mu\text{s}$ trapezoidal pulses, each with $10\ \mu\text{s}$ rise and fall times. All measurements were done on $50\ \mu\text{m} \times 50\ \mu\text{m}$ devices.

Density functional theory (DFT)

Density functional theory (DFT) calculations were performed using the Vienna Ab initio Simulation Package (VASP).⁵⁴⁻⁵⁷ The electron–core interactions were described using the local density approximation (LDA)^{58,59} in conjunction with Blöchl’s projector augmented wave (PAW) method.^{57,60} A plane-wave cutoff energy of 500 eV was employed, and k-point meshes were sampled using the Monkhorst-Pack (MP)⁶¹ method with an $8 \times 8 \times 8$ for conventional unit cells. Atomic positions were fully relaxed until the total energy and interatomic forces

converged to less than 10–8 eV and 0.01 eV/Å, respectively. Vibrational free energies were obtained using the finite displacement method as implemented in Phonopy,⁶² which enabled accurate computation of Helmholtz free energy. The surface energies were calculated using slab models comprising more than 8 layers with a vacuum region thicker than 15Å. For slab calculations, the k-point meshes of MP method $6\times6\times1$ were used. The film thickness was set to 5 nm. The Helmholtz free energy F was calculated using the following relation :

$$F = U + F^{\text{vib}} + \gamma\Omega$$

where U is the internal energy of bulk system, F^{vib} is the vibrational free energy, γ is the surface energy, and Ω is the surface area.

Supporting Information

XPS of 5nm ALD based WO_{3-x} ; Endurance; Imprint; Retention; Conductivity; Pristine P-V and $I_{\text{sw}}\text{-V}$ characteristics of 5nm ALD based WO_{3-x} device; Deconvoluted GI-XRD peaks of 125°C measurement; Lattice mismatch% of HZO with W, WO_3 and single vacancy-contained WO_3 ; STEM image of WO_3 ; $I_{\text{sw}}\text{-V}$ and P-V of 5nm ALD WO_{3-x} device at 85 and 125°C; $I_{\text{sw}}\text{-V}$ of 6nm ALD based WO_{3-x} device when cooled back to RT from 85 and 125°C; Leakage and trap generation rate with cycling; Energy barrier of HZO phase transition; Vibrational entropies of W and WO_3 ; Switching barrier energy with and without WO_3 .

Author Contribution

N.A and J.C. contributed equally to this work. N.A. designed and performed the experiments and analyzed the results. J.C. and C.H.K. performed DFT calculations and analysis. S.S and Y.-H.K fabricated the devices. S.S., J.C., M.T., C.Z. and P.G.R. assisted with the experiments and data analysis. A.K. and J.H.L. supervised the research. N.A. and J.C.

wrote the manuscript with the inputs from all the authors.

Acknowledgement

This work involving reference and O₂ plasma WO_{3-x} devices was supported by SUPREME, one of the seven SRC-DARPA JUMP 2.0 centers. The work with ALD WO_{3-x} devices was supported by the Center for 3D Ferroelectric Microelectronics Manufacturing, an Energy Frontier Research Center funded by the U.S. Department of Energy, Office of Science, Basic Energy Sciences, under Award No. DE-SC0021118. Fab was done at the IMS at Georgia Tech, supported by the NSF-NNCI program (ECCS-1542174). DFT work was supported by National Research Foundation of Korea (RS-2023-00218799, RS-2024-00404361, RS-2023-00257666, RS-2025-24535610), Industrial Technology Innovation Program (RS-2025-06642983), Korea Institute for Advancement of Technology (KIAT) grant funded by the Korea Government (MOTIE) (P0023703, HRD Program for Industrial Innovation) and National Supercomputing Center with supercomputing resources including technical support (KSC-2022-CRE-0075, KSC-2022-CRE-0454, KSC-2022-CRE-0456, KSC-2023-CRE-0547, KSC-2024-CRE-0545).

References

- (1) Khan, A. I.; Keshavarzi, A.; Datta, S. The future of ferroelectric field-effect transistor technology. *Nature Electronics* **2020**, *3*, 588–597.
- (2) Mikolajick, T.; Slesazeck, S.; Park, M. H.; Schroeder, U. Ferroelectric hafnium oxide for ferroelectric random-access memories and ferroelectric field-effect transistors. *Mrs Bulletin* **2018**, *43*, 340–346.
- (3) Das, D. et al. Experimental demonstration and modeling of a ferroelectric gate stack

with a tunnel dielectric insert for NAND applications. 2023 International Electron Devices Meeting (IEDM). 2023; pp 1–4.

(4) Ramaswamy, N.; Calderoni, A.; Zahurak, J.; Servalli, G.; Chavan, A.; Chhajed, S.; Balakrishnan, M.; Fischer, M.; Hollander, M.; Ettiserry, D.; others NVDRAM: A 32Gb dual layer 3D stacked non-volatile ferroelectric memory with near-DRAM performance for demanding AI workloads. 2023 International Electron Devices Meeting (IEDM). 2023; pp 1–4.

(5) Huang, Y.; Wu, Q.; Gong, T.; Yang, J.; Luo, Q.; Liu, M. Bayesian Neural Network with Unified Entropy Source and Synapse Weights Using 3D 16-Layer Fe-Diode Array. *Nature Communications* **2025**, *16*, 8063.

(6) Chavan, A.; Rajagopal, A.; Yan, Y.; Asano, I.; Ettiserry, D.; Antonov, V.; Servalli, G.; Calderoni, A.; Ramaswamy, N. Materials Engineering for High Performance Ferroelectric Memory. 2024 IEEE International Memory Workshop (IMW). 2024; pp 1–4.

(7) Agnesina, A.; Brunion, M.; Kim, J.; Garcia-Ortiz, A.; Milojevic, D.; Catthoor, F.; Perumkunnil, M.; Lim, S. K. Power, Performance, Area and Cost Analysis of Memory-on-Logic Face-to-Face Bonded 3D Processor Designs. 2021 IEEE/ACM International Symposium on Low Power Electronics and Design (ISLPED). 2021; pp 1–6.

(8) Zhang, Y.; Sarvey, T. E.; Bakir, M. S. Thermal challenges for heterogeneous 3D ICs and opportunities for air gap thermal isolation. 2014 International 3D Systems Integration Conference (3DIC). 2014; pp 1–5.

(9) Zhou, M.; Prodromou, A.; Wang, R.; Yang, H.; Qian, D.; Tullsen, D. Temperature-aware dram cache management—relaxing thermal constraints in 3-d systems. *IEEE Transactions on Computer-Aided Design of Integrated Circuits and Systems* **2019**, *39*, 1973–1986.

(10) Micron Technology, Inc. Automotive LPDDR5 SDRAM: x16, Dual-Die Package (DDP), Quad-Die Package (QDP), and Eight-Die Package (8DP). https://lv.mouser.com/datasheet/2/671/Micron_05092023_315b_y4bm_ddp_qdp_8dp_auto_lpddr5_-3175609.pdf?, 2023.

(11) Böscke, T.; Teichert, S.; Bräuhaus, D.; Müller, J.; Schröder, U.; Böttger, U.; Mikolajick, T. Phase transitions in ferroelectric silicon doped hafnium oxide. *Applied Physics Letters* **2011**, *99*.

(12) Mehmood, F.; Mikolajick, T.; Schroeder, U. Wake-Up Mechanisms in Ferroelectric Lanthanum-Doped $\text{HfO}_{0.5}\text{ZrO}_{0.5}\text{O}_2$ Thin Films. *physica status solidi (a)* **2020**, *217*, 2000281.

(13) Park, M. H.; Chung, C.-C.; Schenk, T.; Richter, C.; Hoffmann, M.; Wirth, S.; Jones, J. L.; Mikolajick, T.; Schroeder, U. Origin of temperature-dependent ferroelectricity in Si-doped HfO_2 . *Advanced Electronic Materials* **2018**, *4*, 1700489.

(14) Mimura, T.; Shimizu, T.; Sakata, O.; Funakubo, H. Large thermal hysteresis of ferroelectric transition in HfO_2 -based ferroelectric films. *Applied Physics Letters* **2021**, *118*.

(15) Schroeder, U.; Mittmann, T.; Materano, M.; Lomenzo, P. D.; Edgington, P.; Lee, Y. H.; Alotaibi, M.; West, A. R.; Mikolajick, T.; Kersch, A.; others Temperature-Dependent Phase Transitions in $\text{Hf}_x\text{Zr}_{1-x}\text{O}_2$ Mixed Oxides: Indications of a Proper Ferroelectric Material. *Advanced Electronic Materials* **2022**, *8*, 2200265.

(16) Mittmann, T.; Materano, M.; Chang, S.-C.; Karpov, I.; Mikolajick, T.; Schroeder, U. Impact of oxygen vacancy content in ferroelectric HZO films on the device performance. 2020 IEEE International Electron Devices Meeting (IEDM). 2020; pp 18–4.

(17) Hoffmann, M.; Schroeder, U.; Künneth, C.; Kersch, A.; Starschich, S.; Böttger, U.; Mikolajick, T. Ferroelectric phase transitions in nanoscale HfO_2 films enable giant

pyroelectric energy conversion and highly efficient supercapacitors. *Nano Energy* **2015**, *18*, 154–164.

(18) Lin, Y.-D.; Yeh, P.-C.; Dai, J.-Y.; Su, J.-W.; Huang, H.-H.; Cho, C.-Y.; Tang, Y.-T.; Hou, T.-H.; Sheu, S.-S.; Lo, W.-C.; Chang, S.-C. Highly Reliable, Scalable, and High-Yield HfZrO_x FRAM by Barrier Layer Engineering and Post-Metal Annealing. 2022 International Electron Devices Meeting (IEDM). 2022; pp 32.1.1–32.1.4.

(19) Sünbül, A.; Lehninger, D.; Hoffmann, R.; Olivo, R.; Prabhu, A.; Schöne, F.; Kühnel, K.; Döllgast, M.; Haufe, N.; Roy, L.; others Impact of Ferroelectric Layer Thickness on Reliability of Back-End-of-Line-Compatible Hafnium Zirconium Oxide Films. *Advanced Engineering Materials* **2023**, *25*, 2201124.

(20) Ravikumar, P. G.; Ravindran, P. V.; Aabrar, K. A.; Song, T.; Kirtania, S. G.; Das, D.; Park, C.; Afrose, N.; Tian, M.; Yu, S.; others Comprehensive Time Dependent Dielectric Breakdown (TDDB) Characterization of Ferroelectric Capacitors Under Bipolar Stress Conditions. 2024 IEEE International Reliability Physics Symposium (IRPS). 2024; pp 1–5.

(21) Chen, H.-Y.; Mo, C.-L.; Shyue, J.-J.; Huang, T.-Y.; Chen, M.-J. Probing Hf_{0.5}Zr_{0.5}O₂ Ferroelectricity: Neutron Reflectivity Reveals Critical Interface Effects. *ACS Applied Materials & Interfaces* **2025**, *17*, 16102–16110, PMID: 40021470.

(22) Chen, G.-H.; Liao, Y.-T.; Zhao, Z.; Chen, Y.-R.; Chen, Y.-W.; Chen, W.-J.; Hsu, W.-T.; Lu, H.-Y.; Liu, M.-C.; Chen, Y.-A.; others Uniform and Fatigue-Free Ferroelectric HZO with Record EBD of 6.3 MV/cm and Record Final 2Pr of 64 μC/cm² at Record 5E12 Endurance Using Low Lattice Misfit (2.9%) β -W. 2024 IEEE International Electron Devices Meeting, IEDM 2024. 2024; pp 1–4.

(23) Alcala, R.; Materano, M.; Lomenzo, P. D.; Vishnumurthy, P.; Hamouda, W.; Dubourdieu, C.; Kersch, A.; Barrett, N.; Mikolajick, T.; Schroeder, U. The electrode-

ferroelectric interface as the primary constraint on endurance and retention in HZO-based ferroelectric capacitors. *Advanced functional materials* **2023**, *33*, 2303261.

(24) Wang, X.; Wen, Y.; Wu, M.; Cui, B.; Wu, Y.-S.; Li, Y.; Li, X.; Ye, S.; Ren, P.; Ji, Z.-G.; Lu, H.-L.; Wang, R.; Zhang, D. W.; Huang, R. Understanding the Effect of Top Electrode on Ferroelectricity in Atomic Layer Deposited Hf0.5Zr0.5O2 Thin Films. *ACS Applied Materials & Interfaces* **2023**, *15*, 15657–15667.

(25) Wang, X.; Slesazeck, S.; Mikolajick, T.; Grube, M. Modulation of Oxygen Content and Ferroelectricity in Sputtered Hafnia-Zirconia by Engineering of Tungsten Oxide Bottom Electrodes. *Advanced Electronic Materials* **2024**, 2300798.

(26) Kashir, A.; Kim, H.; Oh, S.; Hwang, H. Large Remnant Polarization in a Wake-Up Free Hf0.5Zr0.5O2 Ferroelectric Film through Bulk and Interface Engineering. *ACS Applied Electronic Materials* **2021**, *3*, 629–638.

(27) Feng, Y.; Wang, X.; He, Y.; Kang, Y.; Zhang, D.; Shi, W.; Zheng, Z.; Jiao, L.; Zhou, Z.; Sun, C.; others Record-High \mathbf{P}_r ($2\mathbf{P}_r > 40 \mu\text{C}/\text{cm}^2$) in 3 nm (Physical) Ferroelectric HZO Annealed at 450 °C: High-T (85 °C) Electrical Cycling and Oxygen Vacancy Engineering. 2025 Symposium on VLSI Technology and Circuits (VLSI Technology and Circuits). 2025; pp 1–3.

(28) Yang, K.; Kim, G.-Y.; Ryu, J. J.; Lee, D. H.; Park, J. Y.; Kim, S. H.; Park, G. H.; Yu, G. T.; Kim, G. H.; Choi, S. Y.; others Wake-up-mitigated giant ferroelectricity in Hf0. 5Zr0. 5O2 thin films through oxygen-providing, surface-oxidized W electrode. *Materials Science in Semiconductor Processing* **2023**, *164*, 107565.

(29) Lee, J.; Song, M. S.; Jang, W.-S.; Byun, J.; Lee, H.; Park, M. H.; Lee, J.; Kim, Y.-M.; Chae, S. C.; Choi, T. Modulating the ferroelectricity of hafnium zirconium oxide ultrathin films via interface engineering to control the oxygen vacancy distribution. *Advanced Materials Interfaces* **2022**, *9*, 2101647.

(30) Shi, S. et al. Interface-engineered ferroelectricity of epitaxial Hf_{0.5}Zr_{0.5}O₂ thin films. *Nature Communications* **2023**, *14*, 1780.

(31) Lehninger, D.; Prabhu, A.; Sünbül, A.; Ali, T.; Schöne, F.; Kämpfe, T.; Biedermann, K.; Roy, L.; Seidel, K.; Lederer, M.; others Ferroelectric [HfO₂/ZrO₂] superlattices with enhanced polarization, tailored coercive field, and improved high temperature reliability. *Advanced Physics Research* **2023**, *2*, 2200108.

(32) Popovici, M.; Bizindavyi, J.; Favia, P.; Clima, S.; Alam, M. N. K.; Ramachandran, R.; Walke, A.; Celano, U.; Leonhardt, A.; Mukherjee, S.; others High performance La-doped HZO based ferroelectric capacitors by interfacial engineering. 2022 International Electron Devices Meeting (IEDM). 2022; pp 6–4.

(33) Itoya, Y.; Saraya, T.; HIRAMOTO, T.; Kobayashi, M. Enhanced reliability of ferroelectric Hf_{0.5}Zr_{0.5}O₂ capacitors by bottom electrode surface oxidation. *Japanese Journal of Applied Physics* **2024**,

(34) Koroleva, A. A.; Chernikova, A. G.; Zarubin, S. S.; Korostylev, E.; Khakimov, R. R.; Zhuk, M. Y.; Markeev, A. M. Retention Improvement of HZO-Based Ferroelectric Capacitors with TiO₂ Insets. *ACS Omega* **2022**, *7*, 47084–47095.

(35) Chen, J.; Xu, J.; Gong, Z.; Gu, J.; Yu, X.; Jin, C.; Peng, Y.; Liu, Y.; Chen, B.; Cheng, R.; others Controlling the Ferroelectricity of Doped-HfO₂ via Reversible Migration of Oxygen Vacancy. *IEEE Transactions on Electron Devices* **2023**, *70*, 1789–1794.

(36) Aich, A.; Senapati, A.; Lou, Z.-F.; Chen, Y.-P.; Huang, S.-Y.; Maikap, S.; Lee, M.-H.; Liu, C. W. Low Voltage High Polarization by Optimizing Scavenged WN_x Interfacial Capping Layer at the Ru/HfxZr_{1-x}O₂ Interface and Evidence of Fatigue Mechanism. *Advanced Materials Interfaces* **2024**, *11*, 2400185.

(37) Hwang, S.; Jang, H.; Lee, K.; Jung, L.; Yoon, J.; Kwon, J.-D.; Song, K.; Kim, Y.; Hwang, H. Record Endurance (> 1012 Cycles), High Polarization (2Pr > 50 μ C/cm²),

and 10-Year Data Retention (85°C) in HZO Capacitors with Well-Ordered Ferroelectric Domain Structures via 2D-WS2 Interface. 2024 IEEE International Electron Devices Meeting (IEDM). 2024; pp 1–4.

(38) Kwon, D. S.; Bizindavyi, J.; De, G.; Belmonte, A.; Delabie, A.; Nyns, L.; Kar, G. S.; Van Houdt, J.; Popovici, M. I. Improvement of the Ferroelectric Response of La-Doped Hafnium Zirconium Oxide Employing Tungsten Oxide Interfacial Layer with Back-End-of-Line Compatibility. *ACS Applied Materials & Interfaces* **2024**, *16*, 41704–41715.

(39) Choi, Y.; Shin, J.; Min, J.; Moon, S.; Chu, D.; Han, D.; Shin, C. Oxygen reservoir effect of Tungsten trioxide electrode on endurance performance of ferroelectric capacitors for FeRAM applications. *Scientific Reports* **2024**, *14*, 28912.

(40) Chiniwar, S. P.; Hsieh, Y.-C.; Shih, C.-H.; Teng, C.-Y.; Yang, J.-L.; Hu, C.; Lin, B.-H.; Tang, M.-T.; Tseng, Y.-C. Ferroelectric Enhancement in a TiN/Hf_{1-x}Zr_xO₂/W Device with Controlled Oxidation of the Bottom Electrode. *ACS Applied Electronic Materials* **2024**, *6*, 1078–1086.

(41) Kim, E.; Park, H.; Jeong, J.; Lim, S.; Woo, J. Comprehensive Reliability Assessment of WO_x Engineering for Temperature-Resilient HfZrO₂ FeCAP. 2025 IEEE International Reliability Physics Symposium (IRPS). 2025; pp 1–5.

(42) Zhao, Z.; Chen, Y.-R.; Chen, Y.-W.; Wang, J.-F.; Xing, Y.; Ji, W.; Chen, G.-H.; Lee, J.-Y.; Dobhal, R.; Liu, C. Engineering Hf 0.5 Zr 0.5 O 2 ferroelectric tunnel junctions with amorphous WO_x bottom electrodes achieving high remanent polarization and record low-operating voltage. *IEEE Transactions on Electron Devices* **2023**, *70*, 5022–5027.

(43) Zhao, C.; Wang, H.; Gu, X.; Zhang, W.; Li, Y. Ultrathin WO_x interfacial layer improving the ferroelectricity and endurance of Hf0.5Zr0.5O₂ thin films on polyimide. *Journal of Materiomics* **2025**, *11*, 100942.

(44) Wang, H.; Qi, J.; Xie, X.; Liu, Z.; Wu, W.; Lee, C. Optimal Process Design for Wake-Up Free $\text{Hf}_{0.5}\text{Zr}_{0.5}\text{O}_2$ Ferroelectric Capacitors: Toward Low-Power Devices with Enhanced Ferroelectric Performance. *Electronics* **2024**, *13*, 2895.

(45) Habibi, M.; Kashir, A.; Schenk, T.; Jang, H.; Oh, S.; Kim, J.; Han, G.; Lee, D.; Koushan, F.; Hwang, H. Highly Reliable $\text{Hf}_1\text{-XZrXO}_2$ with Ultra-Low Operation Voltage (< 1 V) Enabled by Stoichiometric Control of Tungsten Oxide Interfacial Layer. *Advanced Materials Technologies* **2025**, e00507.

(46) Afroze, N.; Padovani, A.; Choi, J.; Ravikumar, P. G.; Kuo, Y.-H.; Zhang, C.; Song, T.; Tian, M.; Sarkar, E.; Noor, M.; others Self-Healing Ferroelectric Capacitors with 1000x Endurance Improvement at High Temperatures (85–125° C). 2024 IEEE International Electron Devices Meeting (IEDM). 2024; pp 1–4.

(47) Padovani, A.; Afroze, N.; Kuo, Y.-H.; Ravikumar, P. G.; Ravindran, P. V.; Tian, M.; Khan, A.; Choi, J.; Lee, J. H.; Larcher, L.; Thareja, G. Multi-Scale Modeling-Driven Material to Device Co-Optimization of Ferroelectric Capacitors with Oxygen Reservoir Layer (ORL) for Improved Endurance. 2025 IEEE International Reliability Physics Symposium (IRPS). 2025; pp 1–6.

(48) Zhang, G.; Wu, H.; Xu, X.; Lin, S.; Zhang, Z.; Yan, Z.; Lu, X.; Yuan, G.; Liu, J.-M. Enhanced reliability of $\text{Hf}_{0.5}\text{Zr}_{0.5}\text{O}_2$ ferroelectric memory through WO_x buffer layer to minimize oxygen vacancies. *Applied Physics Letters* **2025**, *127*.

(49) Yao, Y.; Sang, D.; Zou, L.; Wang, Q.; Liu, C. A Review on the Properties and Applications of WO_3 Nanostructure-Based Optical and Electronic Devices. *Nanomaterials* **2021**, *11*.

(50) Xu, K.; Wang, T.; Liu, Y.; Yu, J.; Liu, Y.; Li, Z.; Meng, J.; Zhu, H.; Sun, Q.; Zhang, D. W.; others La-Doped HZO (La: HZO) Ferroelectric Devices Toward High-Temperature Application. *IEEE Transactions on Electron Devices* **2024**,

(51) Kim, E.; Park, H.; Jeong, J.; Lim, S.; Moon, K.; Woo, J. WO x Interlayer Engineering for Reliable Polarization in HfZrO₂ Ferroelectric Capacitors. *IEEE Transactions on Electron Devices* **2025**,

(52) Wang, W.; Janotti, A.; Van de Walle, C. G. Role of oxygen vacancies in crystalline WO₃. *Journal of Materials Chemistry C* **2016**, *4*, 6641–6648.

(53) Ye, K. H.; Yeu, I. W.; Han, G.; Jeong, T.; Yoon, S.; Kim, D.; Hwang, C. S.; Choi, J.-H. Comprehensive interpretations of thermodynamic and kinetic effects on the phase fractions in Hf_{1-x}Zr_xO₂ by first principle calculations. *Applied Physics Reviews* **2023**, *10*, 031419.

(54) Kresse, G.; Furthmüller, J. Efficient iterative schemes for ab initio total-energy calculations using a plane-wave basis set. *Physical review B* **1996**, *54*, 11169.

(55) Kresse, G.; Hafner, J. Ab initio molecular dynamics for liquid metals. *Physical review B* **1993**, *47*, 558.

(56) Kresse, G.; Furthmüller, J. Efficiency of ab-initio total energy calculations for metals and semiconductors using a plane-wave basis set. *Computational materials science* **1996**, *6*, 15–50.

(57) Kresse, G.; Joubert, D. From ultrasoft pseudopotentials to the projector augmented-wave method. *Physical review b* **1999**, *59*, 1758.

(58) Ceperley, D. M.; Alder, B. J. Ground state of the electron gas by a stochastic method. *Physical review letters* **1980**, *45*, 566.

(59) Perdew, J. P.; Zunger, A. Self-interaction correction to density-functional approximations for many-electron systems. *Physical review B* **1981**, *23*, 5048.

(60) Blöchl, P. E. Projector augmented-wave method. *Physical review B* **1994**, *50*, 17953.

(61) Monkhorst, H. J.; Pack, J. D. Special points for Brillouin-zone integrations. *Physical review B* **1976**, *13*, 5188.

(62) Togo, A.; Tanaka, I. First principles phonon calculations in materials science. *Scripta Materialia* **2015**, *108*, 1–5.

Supporting Information

Figure S1 shows the XPS spectra coming from 5nm ALD deposited WO_{3-x} layer on W bottom electrode and Si substrate. W 4f spectrum shows dominant W^{6+} peaks confirming the formation of WO_{3-x} . Deconvoluted peaks of O 1s spectrum are shown in Figure S1b.

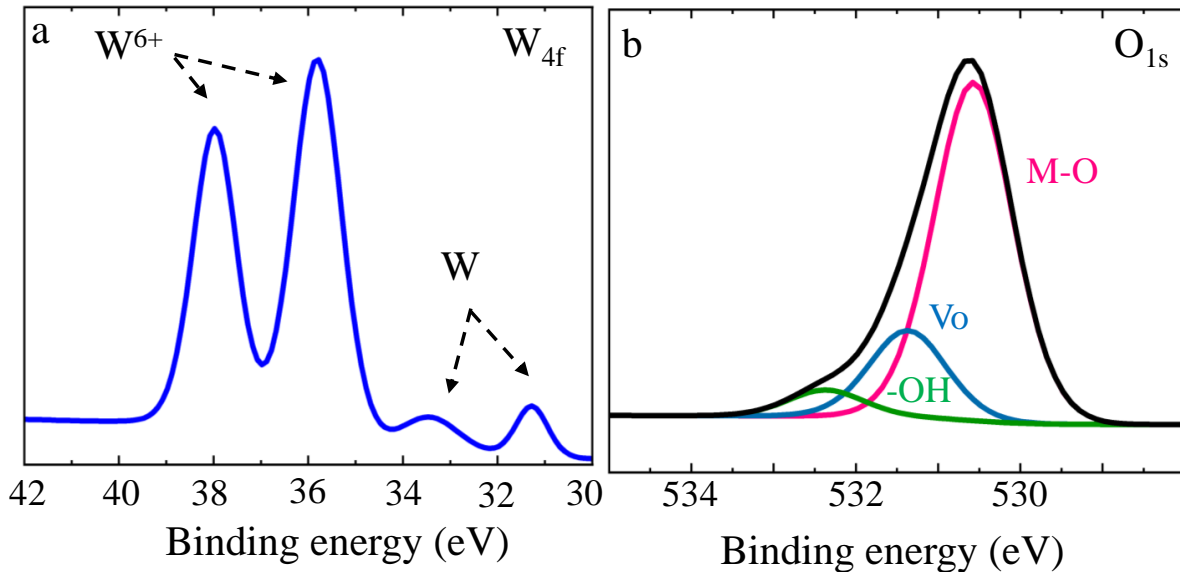


Figure S1: XPS spectra obtained from (a) W 4f and (b) O 1s orbitals of WO_{3-x} from 5 nm ALD grown WO_{3-x} samples. (b) Magenta, blue and green curves are the de-convoluted peaks corresponding to M-O, non-lattice Oxygen (V_o) and -OH respectively.

Figure S2a shows 2P_r versus cycles characteristics at room temperature when 200 ns bipolar pulses of 1.8 V were applied. The reference device lacking WO_{3-x} has poor endurance compared to

both O_2 plasma and ALD based WO_{3-x} devices. WO_{3-x} devices didn't break upto 10^{10} and 10^{11} cycles. The high-temperature endurance characteristics are presented in Figure S2b. Both the O_2 plasma and ALD WO_{3-x} devices exhibit higher endurance than the reference device over a wide temperature range. Although the ALD WO_{3-x} device reaches saturation polarization at 1.8 V (Figure 4g), endurance measurements were also performed using ± 2 V bipolar pulses (orange curve) because of its slightly higher coercive voltage. At least three devices were measured for each condition.

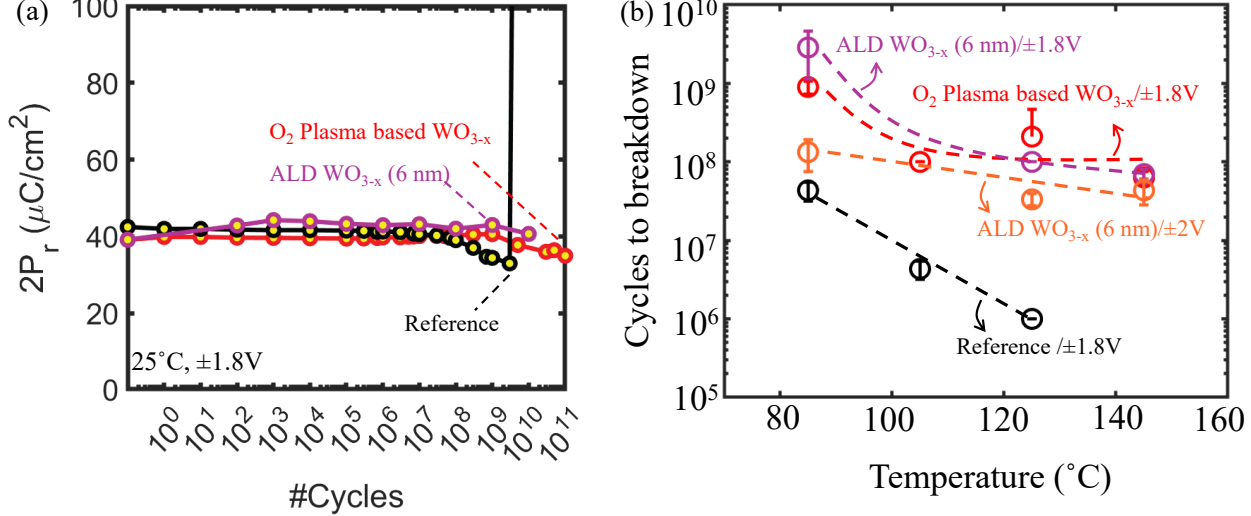


Figure S2: (a) $2P_r$ versus cycles characteristics with bipolar fatigue pulses of ± 1.8 V/200 ns. PV measurements were also done at ± 1.8 V. (b) Cycles to breakdown (endurance) at high temperatures. Both ± 1.8 V and ± 2 V bipolar cycling results are shown for ALD 6nm WO_{3-x} devices.

Figure S3 shows coercive voltage (V_c) versus cycles character-

istics at 125°C when 200ns bipolar pulses of 1.8V were applied.

Imprint doesn't degrade due to the presence of WO_{3-x} compared to

reference device.

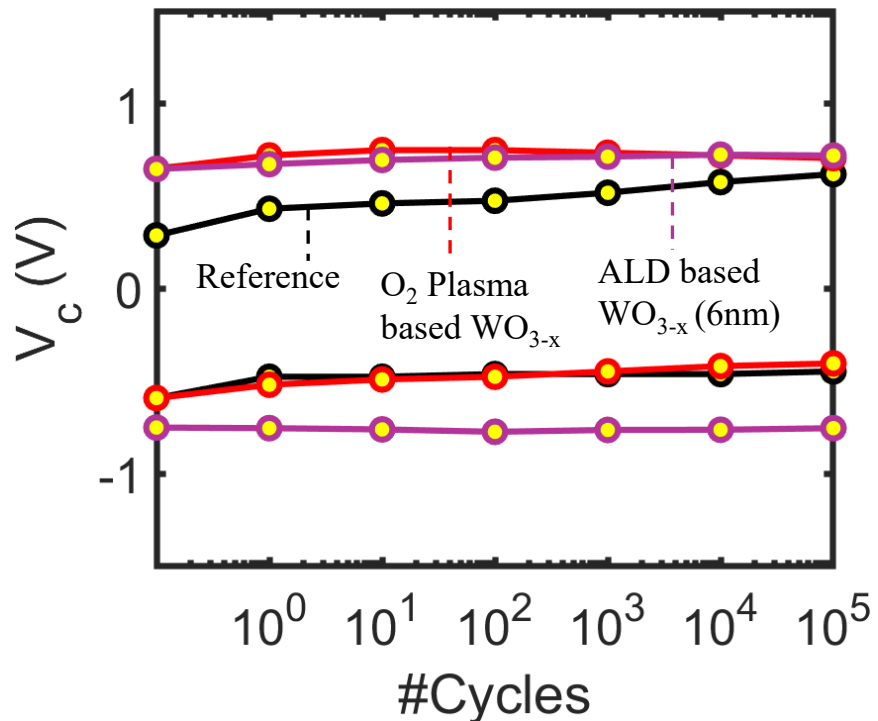


Figure S3: Shift in coercive voltage versus cycles at $\pm 1.8\text{V}/200\text{ ns}$, 125°C .

Figure S4 shows retention characteristics at 85°C by applying $\pm 1.8\text{ V}$ square pulses. Retention doesn't degrade due to the presence of WO_{3-x} compared to reference device.

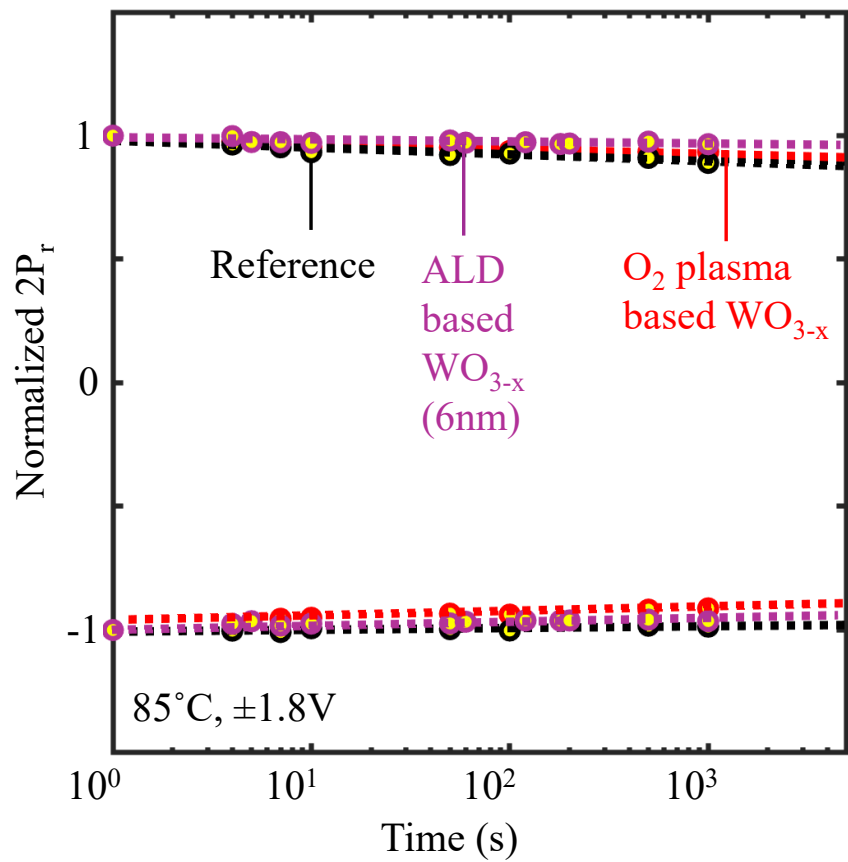


Figure S4: Retention characteristics at 85°C with ± 1.8 V.

Figure S5 shows conductivity of O₂ plasma and ALD based 6 nm WO_{3-x} devices measured on 50 μ m x 50 μ m devices by applying AC voltage of 100kHZ, 25 mV and DC sweep of 1.2 V.

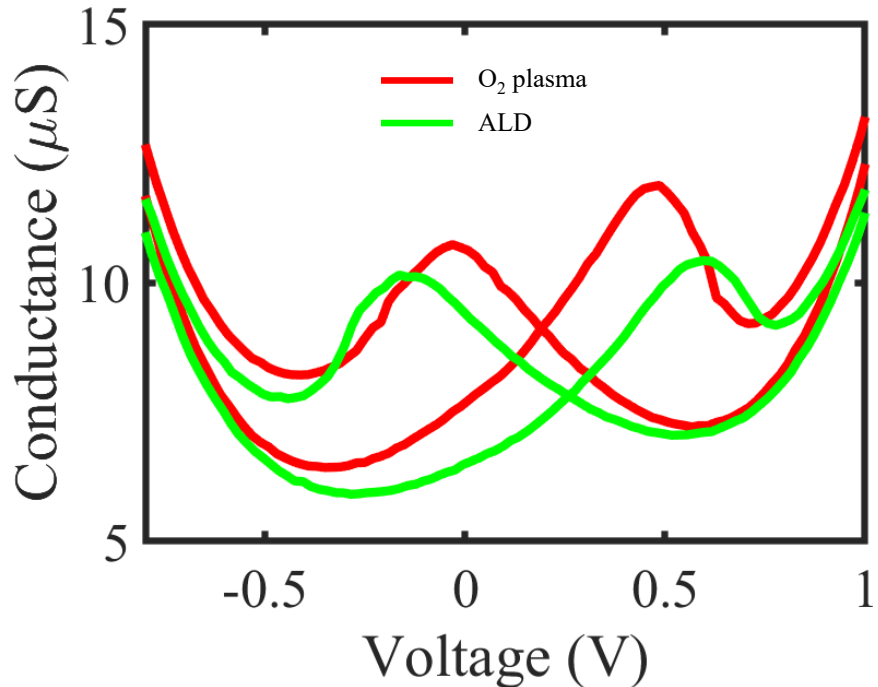


Figure S5: Conductivity versus applied voltage. O₂ plasma based WO_{3-x} device is more conductive compared to ALD based WO_{3-x} device.

Figure S6 shows the P-V and I_{SW}-V characteristics of pristine device measured at different temperatures from 5nm ALD deposited WO_{3-x} device. It shows minimal double peak characteristic (anti-ferro nature) like the 6nm WO_{3-x} device. These measurements were done by applying 1.8V/20μs bipolar triangular pulses.

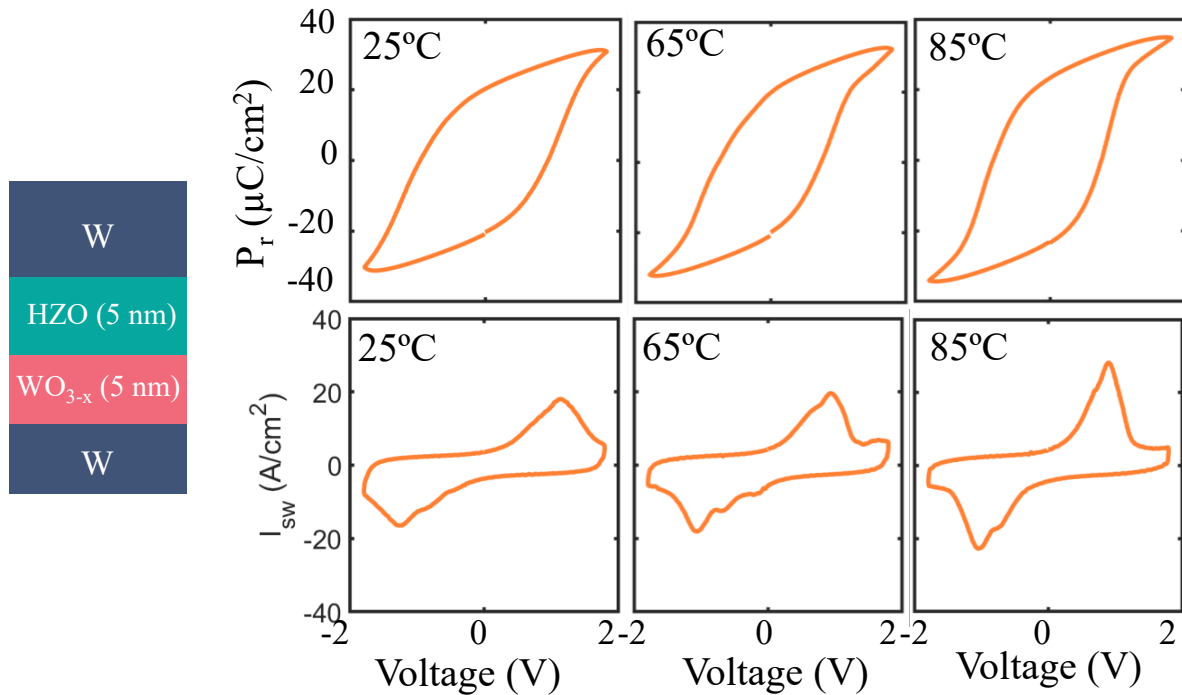


Figure S6: P-V and I_{sw} -V characteristics at 25, 65 and 85°C from pristine ALD deposited 5nm WO_{3-x} device.

Figure S7 presents the deconvolution of the orthorhombic and tetragonal phase components from the Gaussian-fitted o-(111)/t-(101) diffraction peak measured from the HZO layer at 125°C. The ALD-deposited WO_{3-x} sample exhibits the highest orthorhombic phase fraction (73%), whereas the reference sample shows the lowest orthorhombic phase content.

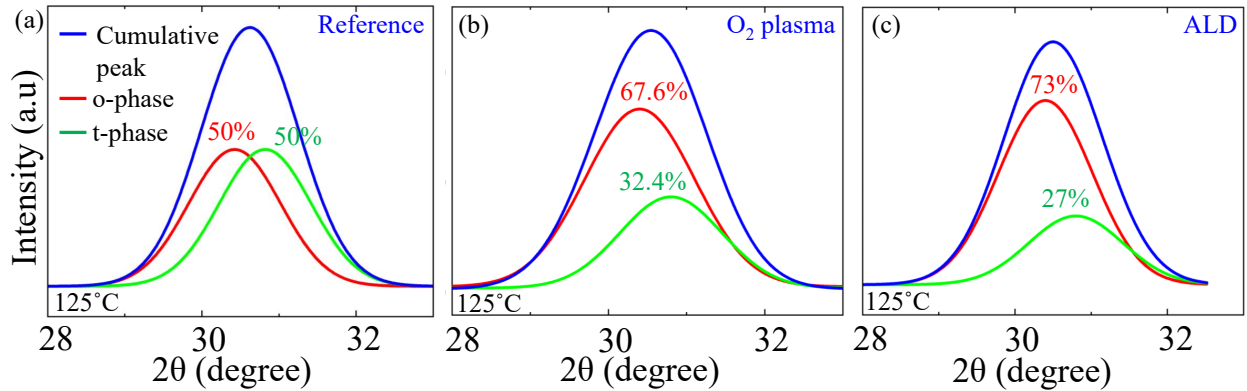


Figure S7: Deconvoluted o- (red) and t- (green) phase peaks from the fitted o-(111)/t-(101) diffraction peak (blue) of the HZO layer for (a) reference, (b) O₂ plasma, and (c) 6nm ALD-deposited WO_{3-x} samples measured at 125 °C.

Table S1 shows lattice constant mismatch of HZO Pca₂₁ (001) and (111) planes with W, WO₃ and 2x2x2 WO₃ supercell containing single Vo²⁺ respectively. The mismatch is lower with both WO₃ and WO_{3-x} compared to W in both a and b directions. Supercell containing vacancy can tune the cell-averaged mismatch while primarily introducing local strain inhomogeneity.⁵² Since HZO (111) plane exhibits a hexagonal geometry, the lattice was matched along the x-axis, and an equivalent magnitude of strain, corresponding to that applied along the x-axis, was imposed along the y-axis to introduce in-plane strain.

Figure S8 shows the HAADF image of WO₃ layer of O₂ plasma device. Fast fourier transform (FFT) of the on-zone grain of WO₃

Table S1: Lattice mismatch (%) of HZO Pca2₁ orientations with W, WO₃ and WO₃ supercell containing single V²⁺.

	W (a)	W (b)	WO ₃ (a)	WO ₃ (b)	WO ₃ - x (a)	WO ₃ - x (b)
HZO Pca2 ₁ (001)	1.76%	5.84%	1.40%	4.07%	1.21%	2.88%
HZO Pca2 ₁ (111)	2.56%		2.48%		2.24%	

confirms it to be m-(001). Overlayed golden W atoms are coming from the crystal structure of monoclinic WO₃ obtained from .cif file of materials project.

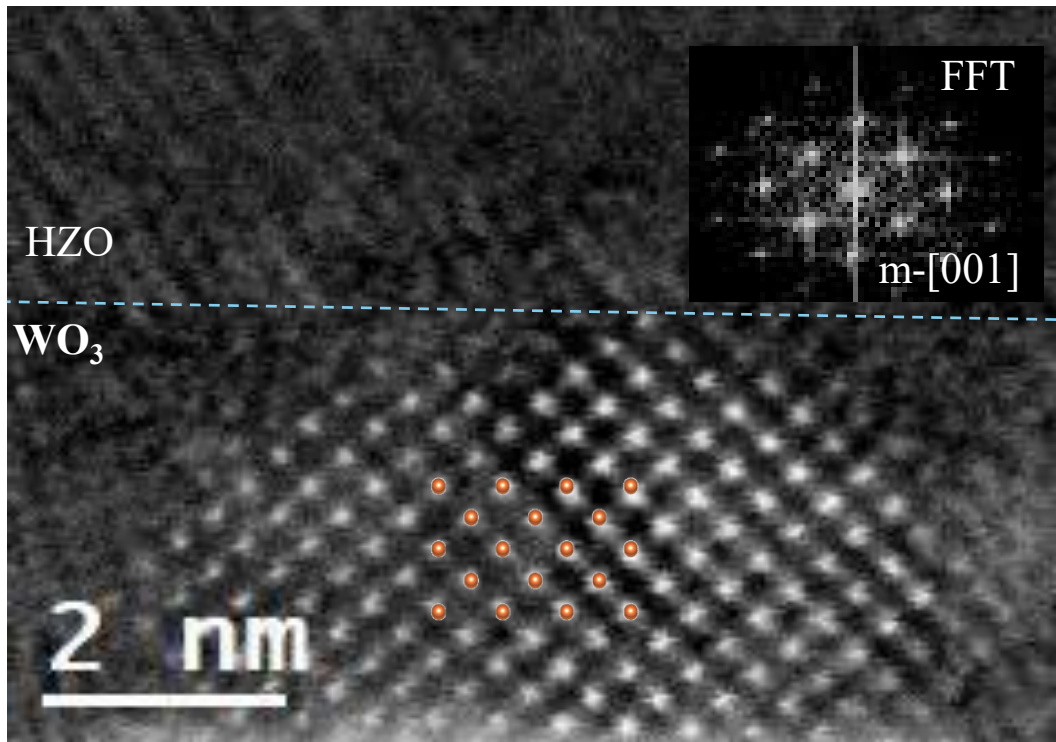


Figure S8: STEM image of WO₃ layer of O₂ plasma based device. Golden Overlayed W atoms are obtained from m-(001) crystal model. Fast Fourier Transform (FFT) of the WO₃ grain confirms it to be m-phase with [001] zone axis.

Figure S9 shows I_{SW}-V characteristics of 5nm ALD deposited WO_{3-x} device measured at 85 and 125°C. Bipolar cycling was done

by applying 200ns/1.8V pulses. Double peak in this device goes away just by applying 10 cycles, similar to 6nm ALD based WO_{3-x} device. Much less cycles are needed for wakeup in devices having WO_{3-x} compared to reference device irrespective of WO_{3-x} thickness.

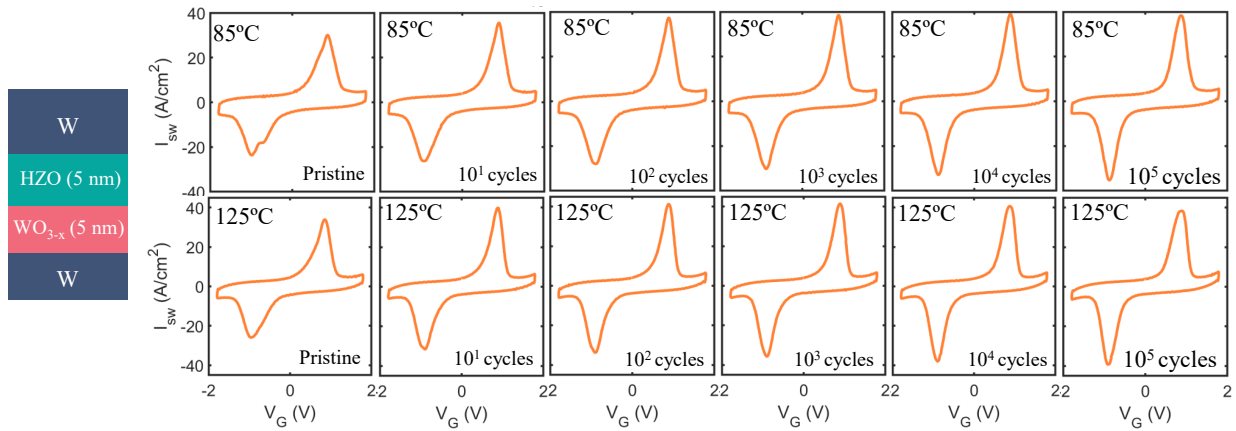


Figure S9: I_{SW} - V characteristics at 85 and 125°C from pristine to 10^5 cycles for ALD deposited 5nm WO_{3-x} device.

Figure S10 shows P-V characteristics with cycling for 5nm ALD based WO_{3-x} device measured at 85 and 125°C respectively. It shows better ferroelectric nature right from the pristine state compared to reference device as shown in Figure 4 (g-h).

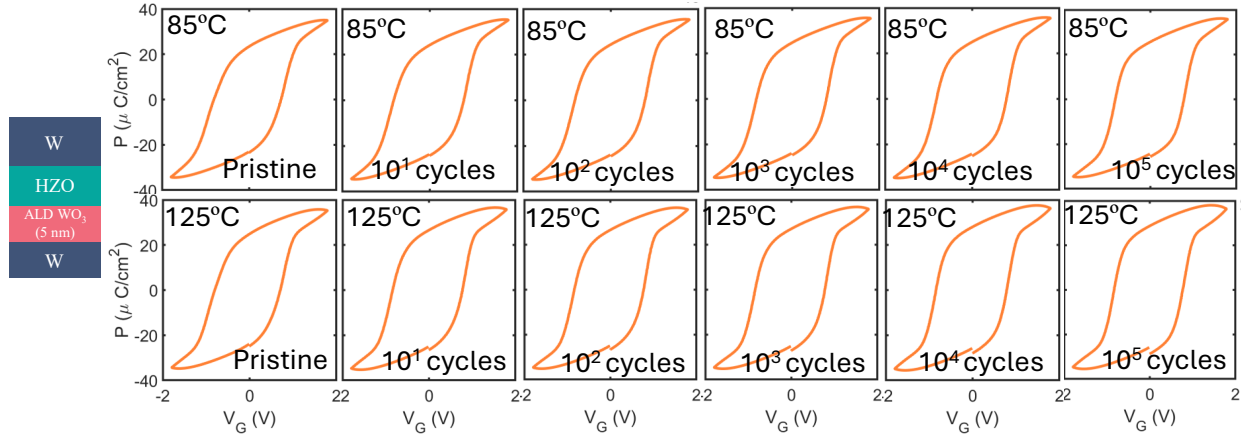


Figure S10: P-V characteristics at 85 and 125°C from pristine to 10^5 cycles for ALD 5nm WO_{3-x} device.

When ten bipolar cycling pulses of ± 1.8 V are applied to the ALD based 6 nm WO_{3-x} device at 85°C and 125°C, the pure ferroelectric switching established at elevated temperatures is well preserved upon cooling to room temperature, as shown in Figure S11.

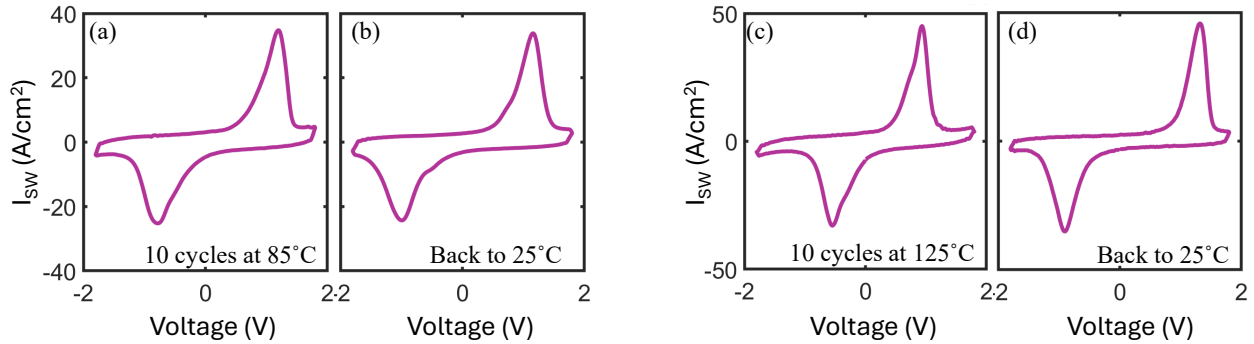


Figure S11: I_{SW} versus voltage characteristics of ALD 6nm WO_{3-x} devices (a) after applying 10 cycles at 85°C and (b) bringing back to 25°C, (c) after applying 10 cycles at 125°C and (d) bringing back to 25°C.

I-V characteristics are measured across a temperature range of

25°C to 125°C up to 5×10^6 cycles, using $\pm 1.7\text{V}$, 200 ns write pulse trains for reference and O_2 plasma devices, and $\pm 1.8\text{V}$, 200 ns pulse trains for ALD devices. The measurements from pristine devices are shown in Figures S12 (a-c). Figures S12 (d-f) show the fractional increase of current density at cycle number = n with respect to the pristine state (n = 0), $\Delta J/J_0 = (J_n - J_0)/J_0$, J_n being the current density at 1V at n-th cycle, as a function of cycle number. The slope of $\Delta J/J_0$ vs. cycles curves (which is a measure of trap generation rate with cycling) is similar at room temperature for all the devices. However, the slope is much lower in all the WO_{3-x} devices at elevated temperatures compared to the reference device.

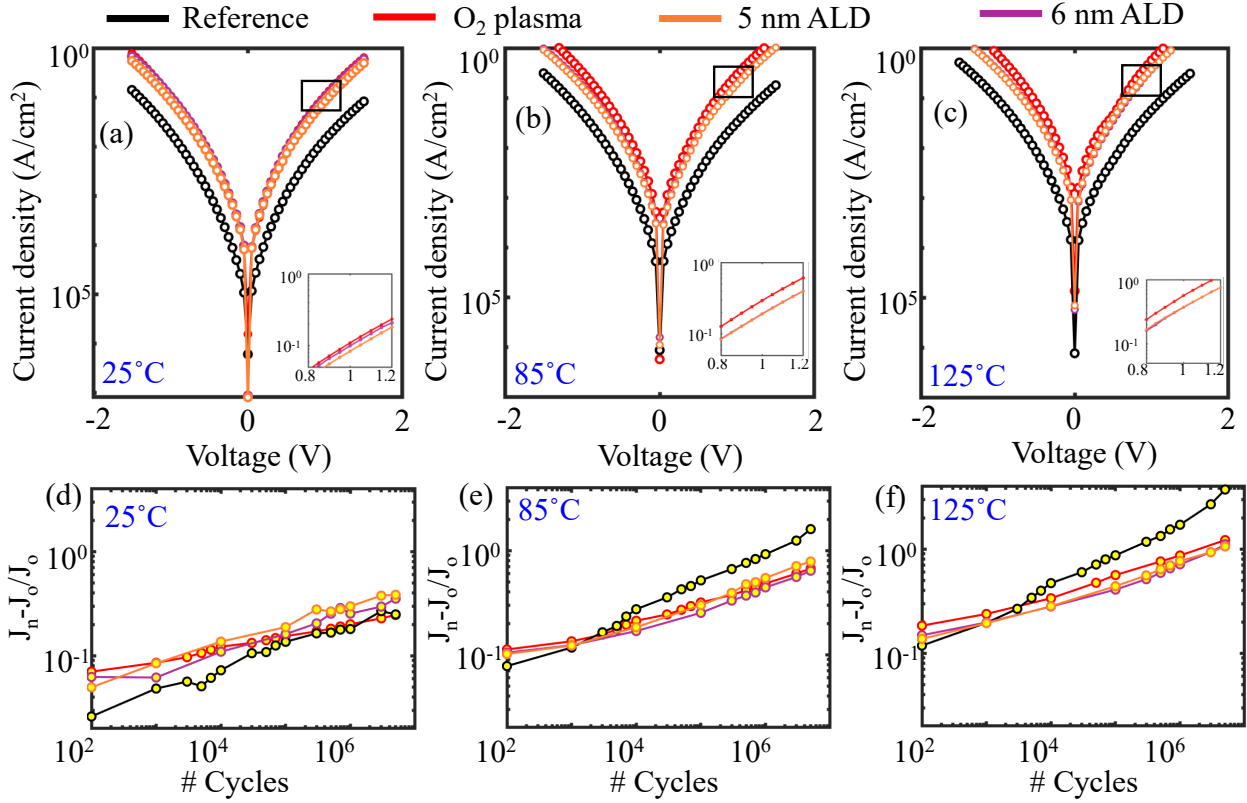


Figure S12: (a-c) Leakage current density versus voltage at pristine state at different temperatures. The insets show the region labeled by the black box. (d-f) $\Delta J/J_0$ with cycling at 1V at (b) 25°C (c) 85°C and (d) 125°C.

Table S2 shows the energy barrier for t-to-m- and t-to-o- phase transition in HZO and HZO strained to W and WO_3 lattices. Transitioning to m- phase is energetically costly than to o- phase from t- phase in all cases.

Figure S13(a) presents the calculated vibrational entropies for the HZO structures matched to the W and WO_3 lattices, respectively. The entropy of the W-matched system is consistently larger

Table S2: Calculated energy barriers for tetragonal-to-monoclinic (t-to-m) and tetragonal-to-orthorhombic (t-to-o) phase transitions.

	Phase transition energy (meV)	
	t-to-m phase	t-to-o phase
HZO	185	77
HZO/WO ₃	176	73
HZO/W	188	69

than that of the WO₃-matched case over the entire temperature range. Figure S13(b) shows the corresponding phonon DOS. As reported previously, the longer interatomic distances lead to softer vibrations, and the softening of phonon modes—manifested as a shift of the phonon DOS toward lower frequencies—results in higher vibrational entropy, since low-frequency vibrations increase the number of accessible vibrational states at finite temperature. Similar behavior in Figure 7a originates from the larger in-plane lattice matched to the W cubic structure under non-equibiaxial strain, which induces softening of the low-frequency phonon modes and consequently increases the vibrational entropy.

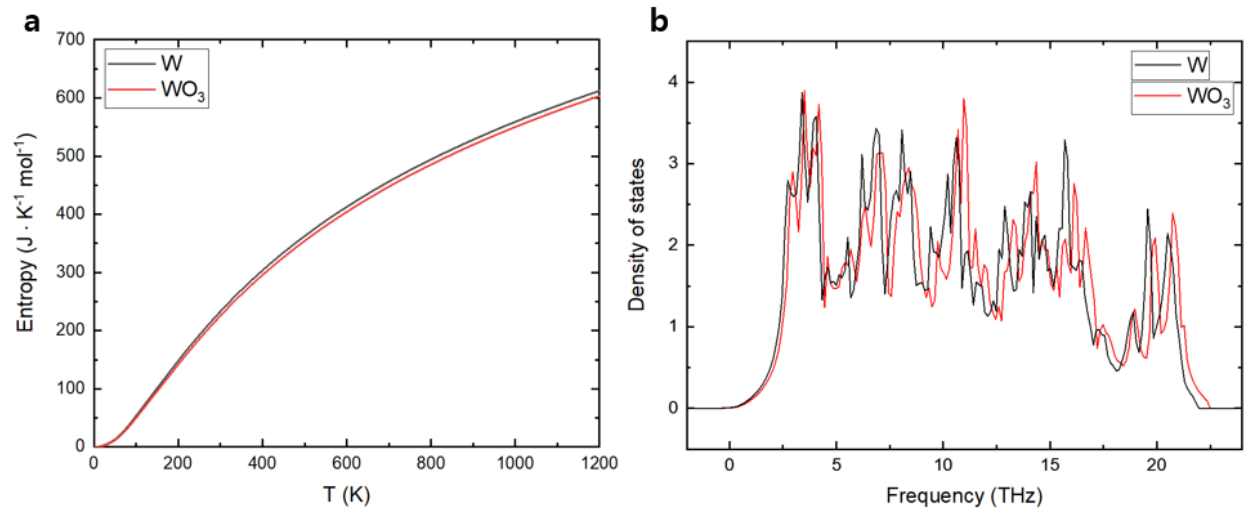


Figure S13: (a) Vibrational entropies for the HZO structures matched to the W and WO_3 lattices. (b) Corresponding phonon density of states (DOS).

In figure S14, it is clear that while transitioning from negative to positive polarization, the energy is higher at $\lambda=0$ for HZO strained to W lattice compared to HZO strained to WO_3 lattice.

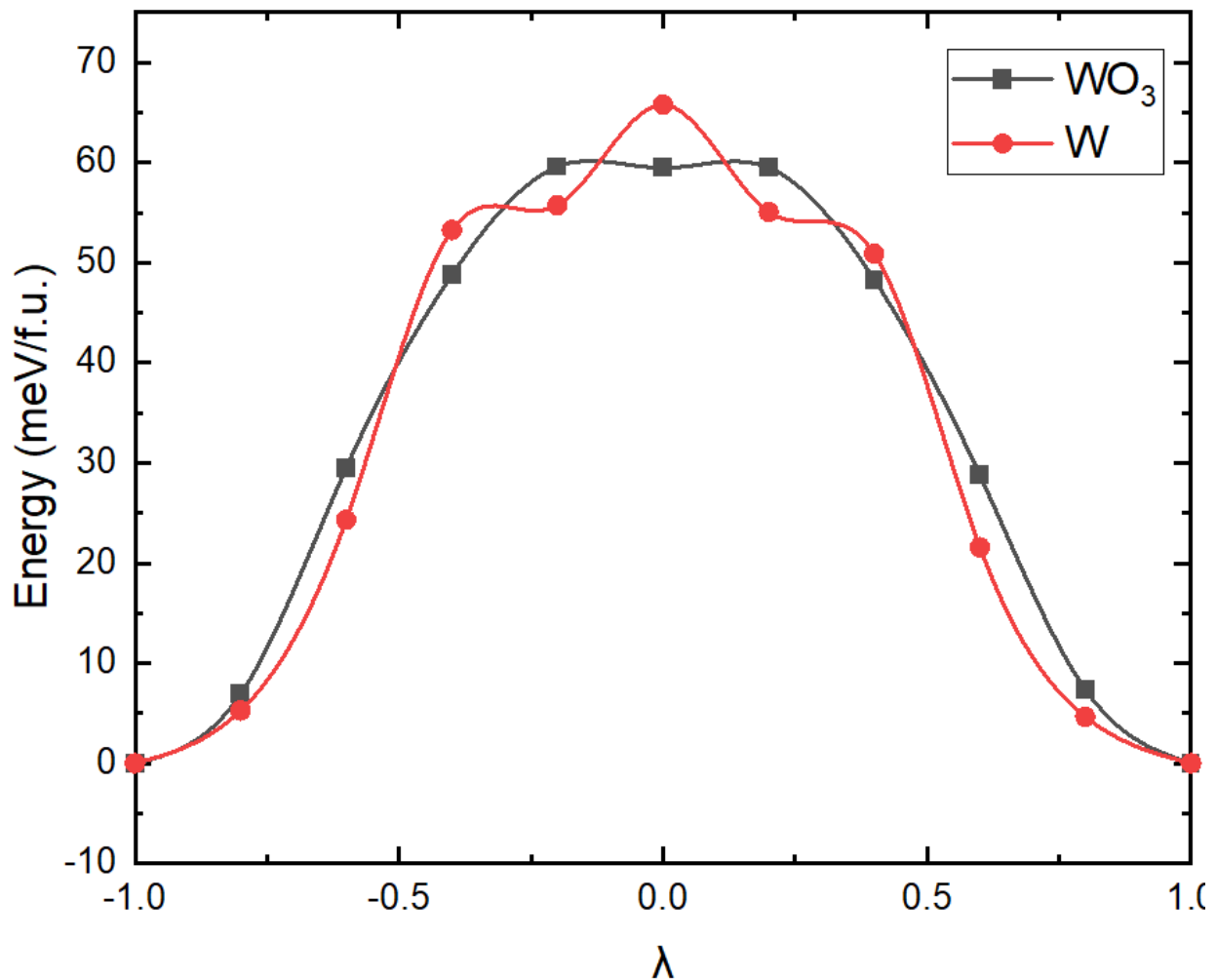


Figure S14: Ferroelectric switching pathways for HZO strained to WO₃ and W lattices. λ denotes the polar displacement, where $\lambda = -1$ corresponds to the ferroelectric (negative) state, $\lambda = 0$ to the paraelectric (zero) state, and $\lambda = 1$ to the ferroelectric (positive) state.